Journal of Petroleum Science and Engineering 169 (2018) 454–470

Contents lists available at ScienceDirect

Journal of Petroleum Science and Engineering

journal homepage: www.elsevier.com/locate/petrol

Temperature effects on rock engineering properties and rock-fluid chemistry in opal-CT-bearing chalk

Mona W. Minde[a,b,*], Wenxia Wang[a,b], Merete V. Madland[a,b], Udo Zimmermann[a,b], Reidar I. Korsnes[a,b], Silvana R.A. Bertolino[c], Pål Ø. Andersen[a,b]

[a] Department of Energy Resources, University of Stavanger, Norway
[b] The National IOR Centre of Norway, University of Stavanger, Ullandhaug, 4036 Stavanger, Norway
[c] Consejo Nacional de Investigaciones Científicas y Técnicas, Instituto de Física Enrique Gaviola, Univ. Nac. de Córdoba, Medina Allende s/n, Ciudad Universitaria, Córdoba, Argentina

ARTICLE INFO

Keywords:
Chalk
Compaction
Dissolution/precipitation
Permeability
Opal-CT
Mineralogical changes

ABSTRACT

In this study, eight tri-axial tests on Cretaceous age outcrop chalk from Aalborg have been performed systematically by injecting $MgCl_2$ for the first time at different temperatures (25, 60, 92, 110 and 130 °C) and for comparison, NaCl at 130 °C. Whole-rock geochemistry, stable isotope measurements, pycnometry, Field Emission Gun Scanning Electron Microscopy with Energy-Dispersive X-ray Spectroscopy, X-Ray Diffraction (XRD) and measurements of Specific Surface Area (Brunauer-Emmett-Teller theory (N_2)) were applied to analyse unflooded and flooded cores. Based on analyses of changes in brine composition, mineralogy, specific surface area, solid density, porosity and permeability some conclusions can be drawn on temperature effects on rock engineering properties and rock-fluid chemistry.

The $MgCl_2$ flooded cores show systematically higher creep rates at higher temperature and the cores tested at 25 and 60 °C show similar creep rates as the two NaCl flooded cores at 130 °C. All fluid-rock interactions were more pronounced at higher temperature. After flooding with $MgCl_2$ at 110 and 130 °C newly formed magnesite is observed. In the cores tested at 25, 60 and 92 °C magnesite crystals have not been positively identified, but minute increases in MgO in whole-rock geochemistry analyses are seen. Si^{4+} originating from the dissolution of silica bearing phases (mainly diagenetic opal-CT), has taken part in the re-precipitation of Si-Mg-bearing minerals during $MgCl_2$ injection from 25 to 130 °C, leading to an increase of the specific surface area. This is partly balanced by opal-CT dissolution, which should lower the specific surface area. The flaky Si-Mg-bearing minerals, covering significant portions of the pore surfaces and throats are the main drivers to reduce permeability in cores flooded at high temperatures. Additionally, in NaCl flooded cores where mineralogical changes are minute, the dissolution of parts of the existing opal-CT has lowered the SSA. At high temperatures, the following chemical changes must be carefully acknowledged when porosity reduction is calculated: calcite and opal-CT dissolution and precipitation of new minerals, particularly Mg-bearing minerals. The presence of opal-CT strongly influences the mineralogical alterations in flooded cores, hence the geo-mechanical evolution.

1. Introduction

Fluid injection into hydrocarbon reservoirs is one of the most often used methods for Enhanced Oil Recovery (EOR). The chemical fluid-rock interplay and induced changes in mechanical and petrological properties have led to research towards finding more optimal injection fluids and possibilities of applying optimized water on field scale (André et al., 2007; Hermansen et al., 2000). The relationships between mechanical properties of reservoir chalk and pore fluids have been of significant interest in scientific research and in industry since the Ekofisk field encountered severe subsidence effects, recognized in the 1980s (Hermansen et al., 1997, 2000; Korsnes et al., 2006a; b; 2008; Kristiansen et al., 2005; Madland et al., 2008, 2011; Nagel, 2001; Newman, 1983; Risnes and Flaageng, 1999; Risnes et al., 2005).

Chalk compaction can be affected by effective stresses, pore fluid compositions and testing temperatures (Korsnes et al., 2008; Madland et al., 2011; Megawati et al., 2013; Nermoen et al., 2016). Chemical reactions involving Mg^{2+} causes calcite dissolution and magnesite

* Corresponding author. Department of Energy Resources, University of Stavanger, Norway.
E-mail addresses: mona.w.minde@uis.no (M.W. Minde), wenxia.wang@uis.no (W. Wang), Merete.v.madland@uis.no (M.V. Madland), udo.zimmermann@uis.no (U. Zimmermann), reidar.i.korsnes@uis.no (R.I. Korsnes), silvanarbertolino@gmail.com (S.R.A. Bertolino), pal.andersen@uis.no (P.Ø. Andersen).

https://doi.org/10.1016/j.petrol.2018.05.072
Received 22 January 2018; Received in revised form 17 April 2018; Accepted 28 May 2018
Available online 02 June 2018
0920-4105/

List of parameters

D	Core diameter, mm
K_i	Initial permeability, mD
L	Core length, mm
M	Mass, g
V	Volume, cm^3
$\delta^{13}C$	A measure of the ratio of stable isotopes ^{13}C and ^{12}C, ‰
$\delta^{18}O$	A measure of the ratio of stable isotopes ^{18}O and ^{16}O, ‰
ε	Axial creep strain, %
P	Solid density, cm^3/L
ρ_w	Brine density, cm^3/L
Φ	Porosity, %

Subscripts

Core	Based on the core piece
Dry	Dry sample
End	State after compaction-flooding tests
i	Initial/unflooded state
Sat	Saturated sample
Vol	volume
P	Pore
S	solid

Abbreviations

Na130	NaCl-flooded core at 130 °C for 60 days (corresponding to the unflooded core *Na130-U*)
*Mg**25***	$MgCl_2$-flooded core at 25 °C for 61 days (corresponding to the unflooded core *Mg**25-U***)
*Mg**60***	$MgCl_2$-flooded core at 60 °C for 62 days (corresponding to the unflooded core *Mg**60-U***)
*Mg**92***	$MgCl_2$-flooded core at 92 °C for 60 days (corresponding to the unflooded core *Mg**92-U***)
*Mg**110***	$MgCl_2$-flooded core at 110 °C for 66 days (corresponding to the unflooded core *Mg**110-U***)
*Mg**130***	$MgCl_2$-flooded core at 130 °C for 61 days (corresponding to the unflooded core *Mg**130-U***)
b.d.l.	Below detection limit
BET	Brunauer-Emmett-Teller theory
DI-H_2O	Deionized water
DW	Distilled water
EDS	Energy-dispersive X-ray spectroscopy
FEG-SEM	Field emission gun – scanning electron microscopy
FEP	Fluorinated ethylene propylene
HPLC	High performance liquid chromatography
ICP-MS	Inductively coupled plasma – mass spectrometry
ICS	Ion chromatography system
LOI	Loss on ignition
L*Na**130***	NaCl-flooded Aalborg core at 130 °C for 118 days (corresponding to the unflooded core L*Na**130-U***)
L*Mg**130***	$MgCl_2$-flooded Aalborg core at 130 °C for 115 days (corresponding to the unflooded core L*Mg**130-U***)
LVDT	Linear variable displacement transducer
PID	Proportional integral derivative
PPM	Part per million
PV	Pore volume
SSA	Specific surface area, m^2/g
sup. mat	Supplementary material
TDS	Total dissolved solids, g/L
TEM	Transmission electron microscopy
TOT/C	Total carbon, %
wt%	Weight percent
XRD	X-Ray diffraction

precipitation during $MgCl_2$ injection at 130 °C (Andersen et al., 2017; Madland et al., 2011; Megawati et al., 2015; Wang et al., 2016; Zimmermann et al., 2013, 2015). As temperatures increase, dissolution and precipitation effects increase when injecting seawater (Korsnes et al., 2008; Zhang et al., 2007) or $MgCl_2$ (Nermoen et al., 2016) into chalk. Nermoen et al. (2016) observed that with $MgCl_2$ injection in outcrop chalk from Obourg St. Vaast (Mons, Belgium) chalk, higher compaction was obtained at 130 °C than at 92 °C. Moreover, authors propose that the rate of deformation changes with temperature and is linked to chemical alteration (Hellmann et al., 2002). We also refer to Andersen et al. (2012, 2017), Andersen and Evje (2016) and Evje et al. (2009) for modelling works that couple geochemical reactions with transport to interpret core flooding tests in both pure and impure chalks.

Several authors (Andersen et al., 2017; Fabricius, 2001; Fabricius et al., 2007; Hjuler, 2007; Hjuler and Fabricius, 2009; Madland et al., 2011; Megawati et al., 2011) have highlighted the importance of investigating the role of non-carbonate minerals in brine-chalk systems. Madland et al. (2011) tested outcrop chalk from Liège (Belgium), flooded with 0.1095 mol/L $MgCl_2$ for ~ 17 days. Silicate minerals dissolved and re-precipitated forming a new silicate mineral phase, containing magnesium, with a clay-like appearance observed in SEM images. Nermoen et al. (2016) emphasized that geochemical analyses were required to investigate more alteration details, particularly the role of silicates. High temperature as a primary factor can also increase silica dissolution (Fournier, 1973) and an increase in brine salinity can substantially increase silica dissolution rate during chemical EOR processes (Elraies and Basbar, 2015).

Outcrop chalk collected close to Aalborg (Denmark), which is typically characterised by a relatively high non-carbonate content compared to other onshore chalks (Hjuler and Fabricius, 2009), indicated by a higher SiO_2 content, shows a complex behaviour in chemo-mechanical experiments (Andersen et al., 2017; Megawati et al., 2015). This is, in particular, related to the abundance of opal-CT (SiO_2 nH_2O), instead of the stable mineral quartz (SiO_2), which dominates the non-carbonate content in other outcrop chalks, such as chalks exposed close to Liège, and in the Midwest of the USA (Kansas and Colorado) (Andersen et al., 2017; Hjuler and Fabricius, 2009; Madland et al., 2011; Megawati et al., 2015; Wang et al., 2016). Even though the North Sea reservoir chalk does not typically contain much opal-CT, it is argued that opal-CT is the source for abundant quartz, mainly occurring as chert (as nodules or bands), created through diagenetic processes (Bromley, 1968; Fabricius and Borre, 2007; Hjuler, 2007). Therefore, one of the objectives of this study is to investigate how opal-CT behaves in porous media, under different temperatures.

Due to shortage of core material, laboratory tests are rarely carried out on reservoir rocks from hydrocarbon deposits in the North Sea, but are commonly performed on on-shore chalk. Chalk from exposures is used to gain information during specific engineering tests with injection of fluids with different compositions. Systematic investigations on reservoir cores are generally expensive and difficult due to issues with core-to-core heterogeneity, cleaning, preservation and sample sizes. For fundamental studies, therefore, the application of outcrop samples, preferably drilled from the same block, gives sufficient information for further research and is paramount for all modelling exercises in this field of research. Reservoir conditions can then be mimicked by selecting samples of comparable mineralogy as reservoir chalk, applying similar fluid compositions, pressure and temperature as found in the reservoir. Such studies contribute in the understanding of EOR processes related to injection of fluids not only for the North Sea reservoirs,

but also for comparable geological settings worldwide.

In this study, we present data from cores drilled out of Cretaceous successions at Aalborg (Denmark), a possible geo-mechanical analogue to North Sea reservoir chalk (Hjuler and Fabricius, 2009), using $MgCl_2$ and NaCl as injection brines with focus on the role of temperature when performing identical flooding - compaction tests at different temperatures. Subsequently, we present the resulting rock mechanical parameters, porosity and permeability and elucidate geochemical and mineralogical changes. The aim of this study is to observe and interpret the chemo-mechanical effects during systematic tri-axial tests with $MgCl_2$ injection at 25, 60, 92 (Valhall reservoir temperature), 110 and 130 °C (Ekofisk reservoir temperature) and NaCl injection at 130 °C for the sake of comparison. As NaCl has been considered to be an inert fluid when flooding chalk, the NaCl-tests at 130 °C were performed as benchmark tests, and variations when flooding NaCl with different temperatures is therefore outside the scope of this paper.

2. Experimental procedures and methods

2.1. Core properties and injection brines

Large chalk blocks were sampled from the Rørdal quarry in Aalborg (Denmark) and eight cores were drilled from these blocks for use in this study. The Aalborg chalk was studied earlier in detail regarding petrology, mineralogical and rheological characteristics (Hjuler, 2007; Hjuler and Fabricius, 2009; Lauridsen et al., 2011; Stenestad, 2006; Surlyk et al., 2010). For identification purposes, the cores have been named with the following notations: *Na*: Flooded with NaCl, *Mg*: Flooded with $MgCl_2$, *numbers* indicating which temperature the experiment was conducted under and L: noting the cores flooded a prolonged time, i. e for close to 120 days, while all other cores were flooded for ~60 days. Cores-samples denoted −**U**, points to the unflooded end-pieces of the original cores (Fig. 1a). The flooding rate for all experiments were chosen to approximately one initial pore-volume per day. This is slightly lower than, but comparable to, water-injections rates at field-scale with typical values of 1 ft/day = 0.3048 m/day (Green and Willhite, 1998).

Core properties, prior to flooding (denoted by *i*), such as length (L_i), diameter (D_i), dry mass ($M_{dry,i}$), saturated mass ($M_{sat,i}$), permeability (k_i), porosity (ϕ_i), solid density (ρ_i) and specific surface area (SSA_i) together with flooding time, and flooding rate are summarized in Table 1. The initial porosity (ϕ_i) was calculated by the difference in saturated and dry mass ($M_{sat,i}$ and $M_{dry,i}$, respectively) divided by the density of distilled water (ρ_{dw}) and initial bulk volume ($V_{b,i}$):

$$\phi_i = \frac{(M_{sat,i} - M_{dry,i})}{\rho_{dw} V_{b,i}} \quad (1)$$

The range was 46.8%–47.9%. The initial permeability (k_i) was measured when the hydrostatic loading started, with values in the range of 0.9–2.5 mD. The initial specific surface area (SSA_i), measured on unflooded end pieces (see Fig. 1a), varies between 3.7 m^2/g and 4.9 m^2/g, correlating positively with the abundance of SiO_2. The solid volumes of unflooded material (end pieces, Fig. 1a) were measured by pycnometry and used to calculate solid densities (ρ_i) of the pieces ranging from 2.62 to 2.68 g/cm^3, slightly lower than the density of calcite (2.71 g/cm^3), implying the presence of a lighter phase, opal-CT (ρ = 1.9 – 2.3 g/cm^3). The solid density ($\rho_{core,i}$) of the whole cores which are to be used for flooding (Fig. 1a) was also calculated by Eq. (2):

$$\rho_{core,i} = \frac{M_{dry,i}}{V_{b,i} - (M_{sat,i} - M_{dry,i})/\rho_w} \quad (2)$$

The densities ($\rho_{core,i}$), calculated based on bulk volume $V_{b,i}$ along with dry and saturated masses ($M_{dry,i}$ and $M_{sat,i}$, respectively) and the density of water (ρ_w), are similar to the pycnometry measurements (ρ_i) in cores ***Mg25-U***, ***Mg60-U***, L***Mg130-U*** and L***Na130-U***, but slightly lower in cores ***Mg92-U*** ∤ 0.01 g/cm^3), ***Mg110-U*** ∤ 0.05 g/cm^3), ***Mg130-U*** ∤ 0.02 g/cm^3) and ***Na130-U*** ∤ 0.03 g/cm^3). These deviations can be attributed to the higher amount of uncertainties for whole core calculations, introduced by the large amount of parameters.

2.2. Flooding experiments in standard tri-axial cells

Cylindrical samples were drilled from collected outcrop material. Each sample was divided axially into three parts (Fig. 1a). The central parts were shaped to cylindrical cores with one of two diameters ~37.0 or ~38.1 mm with a length of ~70.0 mm and used for flooding-compaction tests. The two adjacent parts were used for analysis of unflooded material (Fig. 1a).

The cores have a length to diameter ratio close to two as such that their strength can be expected to be insensitive to differences in diameter (see e.g. Fig. 7.2 in Fjær et al., 2008). After preparation, the cores were dried for 12 h in a heating chamber at 100 °C to remove the water before the dry mass was determined. The mineralogy is not affected by the drying conditions (MacDonald, 1956). The cores were then evacuated by vacuum prior to being saturated with distilled water and weighed to obtain the saturated mass. The same experimental procedure was used on all cores. The saturated cores were mounted into identical tri-axial cells. For detailed set-up of the cells, the reader is referred to Andersen et al., 2017. To isolate the cores from the confining oil, a heat shrinkage sleeve (1– ½" FEP with diameter of 33 – 43 mm and 0.5 mm wall thickness) was installed between the core and the confining oil. After mounting the core, the confining pressure was increased to 0.5 MPa. Thereafter the experiments were conducted according to the following stages:

1. The samples were flooded with three pore volumes (PVs) of distilled water (DW) overnight at ambient temperature to clean the sample before the flooding test. This flooding procedure does not significantly alter the geochemical measurements of the core.
2. Change from flooding with DW to $MgCl_2$ or NaCl by attaching the piston cell into the flow loop. The ion compositions of the injected brines are shown in Table 2. Throughout the rest of the test, the flow rate was set to 1 initial PV per day.

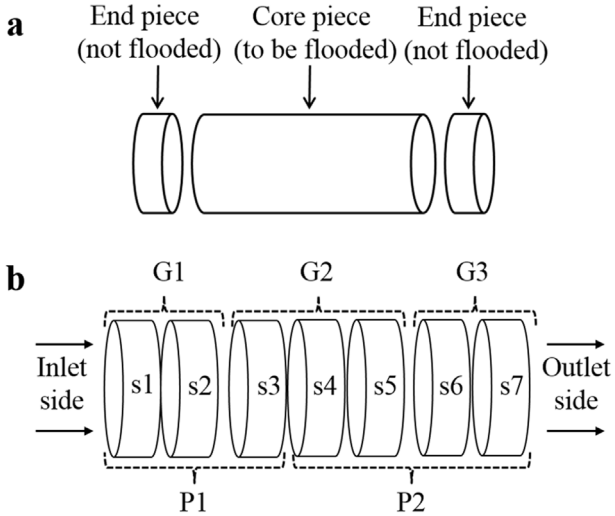

Fig. 1. (A): Material selection procedure: A cylindrical sample is cut into 3 pieces: the central core to be used in flooding-compaction tests and two adjacent end pieces used to measure properties of unflooded material, assumedly also representative of the core. (b): Scheme of the sectioning of the core after the flooding-compaction tests. The cores were cut to two parts (P1, P2) before cut to seven slices (s1, s2 … s7). The inlet is at s1 and the outlet is at s7 (arrows indicate flow direction). The two parts (P1, P2) and slices, grouped into G1 (s1 + s2), G2 (s3 + s4 + s5), and G3 (s6 + s7), were measured by pycnometry. The specific surface area was measured using material from slices s1, s3 and s7.

Table 1
Geo-mechanical properties of the cores applied in the tests before flooding. 'L_i', initial length (mm); 'D_i', initial diameter (mm); $M_{sat,i}$ and $M_{dry,i}$ are saturated and dry mass (g) before flooding, respectively; 'SSA_i', initial specific surface area before flooding (m^2/g); 'k_i', the initial permeability (mD); 'ϕ_i' initial porosity (%), 'ρ_i', initial solid density (g/cm^3) of unflooded material measured by pycnometry and $\rho_{core,i}$ initial solid density (g/cm^3) of whole cores; This difference between ρ_i and $\rho_{core,i}$ might be caused by differences in the vacuum pressure when saturating the cores with distilled water. Flooding rate was 1 pore volume (PV)/day.

Core	L_i	D_i	$M_{sat,i}$	$M_{dry,i}$	Flooding time	Flooding rate	k_i	ϕ_i	ρ_i	$\rho_{core,i}$	SSA_i
	(mm)	(mm)	(g)	(g)	(days)	(ml/min)	(mD)	(%)	(g/cm^3)	(g/cm^3)	(m^2/g)
Mg25-U	71.8	37	143.52	106.62	61	0.026	5.24	47.9	2.65	2.65	4.3
Mg60-U	72.6	37	146.79	110.28	62	0.025	3.46	46.8	2.66	2.66	3.7
Mg92-U	69.2	38.1	147.79	110.74	60	0.026	2.58	47.1	2.66	2.65	4.8
Mg110-U	69.4	37.1	138.44	102.93	66	0.025	2.93	47.4	2.66	2.61	4.8
Mg130-U	70.4	38.1	150.18	112.33	61	0.026	1.52	47.2	2.67	2.65	3.8
L***Mg130-U***	75	38.1	160.43	119.84	115	0.028	1.34	47.5	2.67	2.67	4.9
Na130-U	70.4	38.2	150.64	112.96	60	0.026	2.35	46.9	2.67	2.63	4.5
L***Na130-U***	70.4	37	142.14	106.17	118	0.025	1.79	47.5	2.68	2.68	4.5

Two brines were used for core flooding: 0.219 mol/L $MgCl_2$ and 0.657 mol/L NaCl, (see Table 2). The ionic strength (0.657) was kept the same as in North Sea seawater.

Table 2
Injected brine composition for tests. TDS = total dissolved solids.

Brine	Cl^-	Mg^{2+}	Na^+	Ion strength	TDS
	(mol/L)	(mol/L)	(mol/L)		(g/L)
$MgCl_2$	0.438	0.219	0	0.657	20.84
NaCl	0.657	0	0.657	0.657	38.4

3. The confining pressure and pore pressure were increased simultaneously to 1.2 and 0.7 MPa, respectively before the temperature was raised to the chosen values. The pore pressure and temperature were subsequently kept constant throughout the test.
4. The confining pressure was increased from 1.2 MPa by injecting hydraulic oil at a constant flow rate into the confining chamber using pump 2. During pressurization the piston pressure was set to 0.5 MPa to overcome friction of the piston (0.3 − 0.4 MPa). This increased the axial stress to a value of 0.1 − 0.2 MPa above the radial stress. Because the additional axial stress is small compared to the radial stress, the stress condition can be considered near hydrostatic. The axial strain was measured by an external axial linear variable displacement transducer (LVDT) placed on top of the piston to monitor the sample length with time. The stress-strain behaviour was monitored during the increase in confining pressure. When the rock began to deform plastically, i.e. when the stress strain behaviour became non-linear, the stress at onset of yield was noted until the confining pressure was increased over yield point. The confining pressure was further increased to the chosen creep stress (between 8 and 12 MPa) before the cores where left to compact in the following creep phase (deformation at constant stress).
5. The axial deformation at constant temperature and pressure conditions (termed creep) was monitored during continuous flooding of $MgCl_2$-or NaCl-brine. The pore pressure and confining pressure varied within 0.1 MPa such that the effective stresses were stable throughout the test period.

The pore pressure, hydraulic pressure difference, confining pressure, piston pressure, sample length (axial strain) and flooding time were logged continuously via a LabView program. Before dismantling the core, the sample was cleaned by injection of minimum three PVs of distilled water to avoid precipitation of salts from $MgCl_2$-or NaCl-brines during drying. The saturated weight ($M_{sat,end}$) was measured immediately after the dismantling of the cell. Then the core was placed in the drying cabinet at 100 °C and weighed several times until the dry mass ($M_{dry,end}$) stayed constant. All experiments have been performed in the same way such that the temperature dependent behaviour can be identified. The basic core details before and after flooding are collected in Tables 1, 3–5. Each core was cut to two parts (P1: Part one, to be cut into slice 1, 2 and 3; P2: Part two, to be cut into slice 4, 5, 6, 7, Fig. 1b) to measure the average core solid density ($\rho_{core,avg}$) before cut into the mentioned seven slices (s1, s2, s3, s4, s5, s6 and s7) using a Struers Discotom-5 cutting machine (see Fig. 1b for the sectioning scheme). The slices were used for geological analyses to identify chemical and mechanical changes along the core.

2.3. Field emission gun-scanning electron microscopy (FEG-SEM)

Fresh surfaces from each slice were analysed using a Zeiss Supra 35 VP field emission gun scanning electron microscope (FEG-SEM) in high vacuum mode with an accelerating voltage of 15 kV (occasionally lowered for high resolution images), aperture size of 30 µm, and working distance of 10 − 12 mm. To ensure a steady flux of electrons, the samples were coated with palladium with an Emitec K550 sputtering device. EDAX (Company name) Genesis energy-dispersive X-ray spectroscopy (EDS) was used for determining the mineralogical and elemental composition of the chalk samples. Because the chalk dominantly consists of calcite, the EDS system was calibrated using an Iceland spar calcite crystal. EDS measurements are not presented as independent results, but used as a complementary analysis for changes in elemental composition in the cores and identification of minerals imaged by FEG-SEM.

2.4. X-ray diffraction (XRD)

X–Ray Diffraction patterns were obtained from grinded bulk samples of unflooded material and the different slices of flooded cores (Sup. Mat. Fig. 9). The analyses were performed by using a Bruker D5005 diffractometer (Cu-Kα radiation, 40 kV, 40 mA, 0.02° step, at 1 s per step), at the Institute of Earth Sciences Jaume Almera (ICTJA, Barcelona, Spain), together a Philips X'Pert PRO PW 3040/60 diffractometer (Cu-Kα x-ray radiation, Si monochromator, 40 kV and 30 mA, step scan at ~1.5°/minute, step size of 0.02° 2θ) at the Facultad de Ciencias Químicas (Universidad Nacional de Córdoba, Argentina), and a with a Bruker D8 ADVANCE ECO diffractometer with a Lynxeye detector (Cu-Kα radiation 1.5406 Kα1, 40 kV 25 mA, 0.6 mm receiving slit, 0.01° step, at 0.2 s per step) at the University of Stavanger. The measurements were repeated in certain samples to evaluate the reproducibility of the results; particularly for cases involving newly formed trace minerals. The used amount for measurements was approximately 1 g.

2.5. Whole-rock geochemistry

Representative sample material from each slice was carefully separated from the core and milled to a very fine mesh in a clean agate

mill. Geochemical data were obtained by Inductively Coupled Plasma-Mass Spectrometry (ICP-MS) analysis at Acme laboratory (Vancouver, Canada). Details for the analytical method and processing is compiled here: The milled sample was mixed with $LiBO_2/Li_2B_4O_7$ flux in crucibles and fused in a furnace. The cooled bead was dissolved in the American Chemical Society (ACS) grade nitric acid and analysed by ICP-MS. Loss on ignition (LOI) was determined by igniting a sample split then measuring the weight loss: A 1 g sample was weighed into a tarred crucible and ignited to 1000 °C for 1 h, then cooled and weighed again. The loss in weight is the LOI of the sample. Total Carbon and Sulphur were determined by the Leco method. Here, induction flux was added to the prepared sample then ignited in an induction furnace. A carrier gas sweeps up released carbon to be measured by adsorption in an infrared spectrometric cell. Results are total concentrations and attributed to the presence of carbon and sulphur in all components. An additional 14 elements were measured after dilution in Aqua Regia. The prepared sample was digested with a modified Aqua Regia solution of equal parts concentrated HCl, HNO_3, and DI-H_2O for 1 h in a heating block or hot water bath. The sample volume was increased with dilute HCl-solutions and splits of 0.5 g were analysed. None of the measured concentrations was too far above the possible detection limit, but in standard range, and accuracy and precision are between 2–3%.

2.6. Stable isotope geochemistry (C-O isotope)

Isotope analyses were performed at the University of Edinburgh geological lab and reported by $\delta^{13}C_{SMOW}$ and $\delta^{18}O_{SMOW}$ (isotope ratios with reference to standard mean ocean water (SMOW) composition in Vienna Pee Dee Belemnite). Oxygen and carbon stable isotope analyses were performed on crushed 0.5 −1.0 mg sub-samples. The carbonate powder was reacted with 100% orthophosphoric acid at 90 °C in an ISOCARB automatic carbonate preparation system. The resulting CO_2 was then analysed on a VG Isogas PRISM III stable isotope ratio mass spectrometer. The standard deviation (n = 24) of a powdered coral laboratory standard (COR1D, $\delta^{13}C = -0.647$, $\delta^{18}O = -4.920$) run as a sample on the same days as the study samples, was ± 0.07‰ for $\delta^{13}C$ and ± 0.08‰ for $\delta^{18}O$.

2.7. Ion chromatography

During the flooding experiment, the effluent samples were collected for chemical comparison between the produced and injected water. The ionic concentrations were analysed with a Dionex Ion Chromatography System (ICS)-3000 ion-exchange chromatograph. The analyses were performed with ICS 3000 CD Conductivity Detector. IonPac AS16 and IonPac CS12A were used as anion and cation exchange columns, respectively. The sampled effluents were diluted (Gilson, GX-271) to stay in the linear region of the calibration curve and ionic concentrations were calculated based on an external standard method. The following ion concentrations were quantified: Mg^{2+}, Na^+, Cl^- and Ca^{2+}.

2.8. Inductively coupled plasma-atomic emission spectroscopy (ICP-AES)

The Inductively coupled plasma (ICP) analyses of effluents for measuring Si^{4+} concentrations were performed using the Optima 4300 DV inductively coupled plasma optical emission spectrometry (ICP-OES) detector instrument from Perkin Elmer. The samples were prepared by separating approximately 1 mL of the fluid before dilution. The method detection limit (MDL) for the analysis of Si^{4+} on the machine (University of Stavanger) is 0.3 mg/L.

2.9. Pycnometry

The solid volume was measured with an AccuPyc II 1340 gas pycnometer that measures the amount of displaced helium gas within a porous rock sample. The dry sample was placed into the volume chamber where helium gas molecules rapidly fills the pores enabling measurement of the solid volume filled by the sample. A chamber of 35 cm^3 was selected to provide the best fit with the samples. Based on the measured solid volume and dry mass, estimates of the average mineral densities were obtained. The pycnometry measurements represent a complimentary way of estimating the porosity, in addition to the porosity estimate from the difference between the dry and DW-saturated cores.

2.10. Specific surface area (SSA)

Specific surface area on grinded bulk chalk samples was measured by Micromeritics' TriStar II surface area and porosity analyser and the data was calculated by TriStar II 3020 Software. Each sample was weighed and inserted into a sample tube before the dry sample tube was then carefully connected to vacuum until the vacuum had stabilized (20–30 mTorr). The sample tube was submerged in liquid nitrogen (N_2) to cool the sample during the measurement. At increased partial pressures, nitrogen gas fills a greater area of the micro-pores adsorbing as a monolayer on the surface of the grains. The change in pressure is a measure of the amount of gas adsorbed, thus the surface area of the sample. Given the sample weight as input, the program can calculate the specific surface area of the sample by the Brunauer–Emmett–Teller (BET) theory (Brunauer et al., 1938).

2.11. Porosity estimation

Porosity development within the brine-chalk system can be described by considering mass exchange and mechanical compaction (Nermoen et al., 2015; Wang et al., 2016). In *this* study, we focus on the porosity estimation after flooding; therefore, we apply the methods proposed by Wang et al. (2016), which will be summarized below.

After the experiment was finished and the core dismantled, the diameter (D_j) was measured at intervals (L_j) along the core to estimate the total bulk volume ($V_{b,\,end}$) from the sum of contributions from each slice j = 1, 2 … 7:

$$V_{b,end} = \sum_j \frac{L_j \cdot \pi}{12}((D_j)^2 + (D_j D_{j+1}) + (D_{j+1})^2) \tag{3}$$

The above formula assumes diameters D_j and D_{j+1} are measured at the end faces of slice j (see Fig. 1b) and that the diameter varies linearly in between. The overall change in bulk volume between initial volume ($V_{b,i}$) and the volume after testing ($V_{b,\,end}$, from Eq. (3)) was used to estimate the total volumetric strain ε_{vol}:

$$\varepsilon_{vol} = \frac{V_{b,i} - V_{b,\,end}}{V_{b,i}} \tag{4}$$

End porosity is, by definition, the ratio of pore (p) and bulk (b) volume, where each end volume equals the original volume plus the volume change after testing:

$$\phi_{end} = \frac{V_{p,i} + \Delta V_p}{V_{b,i} + \Delta V_b} = \frac{V_{p,i} + \Delta V_b - \Delta V_s}{V_{b,i} + \Delta V_b} = \frac{\phi_i - \varepsilon_{vol} - \frac{\Delta V_s}{V_{b,i}}}{1 - \varepsilon_{vol}} \tag{5}$$

The change in solid volume is not directly measured, thus porosity will be estimated as discussed in the following.

If all deformation is accommodated by pore volume reduction and the solid volume (s) remains constant ($\Delta V_s = 0$, i.e. $\Delta V_b = \Delta V_p$) (assuming incompressible mineral grains, and either no rock-fluid interactions or that the alteration of mineral density and transport processes preserve the mineralogical mass) then the porosity estimate after flooding is described by:

$$\phi_{end,1} = \frac{V_{p,i} + \Delta V_b}{V_{b,i} + \Delta V_b} = \frac{\phi_i - \varepsilon_{vol}}{1 - \varepsilon_{vol}} \tag{6}$$

As stated, this is theoretically the porosity of the rock, if the solid

Table 3
Geochemical analyses, solid density (in two parts and three groups, g/cm^3, Fig. 1), difference between the current density and average density (2.66 g/cm^3, in bold, italic), specific surface area measurement (m^2/g) and difference between current SSA and initial average SSA$_i$. (a) NaCl flooded cores, (b) $MgCl_2$ flooded cores. The abbreviations are 'PPM' for part per million 'wt%' for weight percent, 'T', temperature estimation, °C, and 'TOT/C' total carbon, 'I.S.': not analysed because of insufficient sample for analyses after cutting,*: not analysed by the given method or not applicable. For each unflooded sample, $\delta^{13}C_{SMOW}$ and $\delta^{18}O_{SMOW}$ respectively are average of two measurements. SMOW (standard mean ocean water) is given in per mil (‰). Temperatures have been calculated after Anderson and Arthur (1983) with salinity values by Wright (1987).

(a) NaCl flooded	SiO_2	MgO	CaO	$\delta^{13}C_{SMOW}$	$\delta^{18}O_{SMOW}$	T	SSA	ΔSSA	sample	ρ_{end}	sample	ρ_{end}
	(wt%)	(wt%)	(wt%)	(‰)	(‰)	(°)	m^2/g	m^2/g		g/cm^3		g/cm^3
Na130-U	5.0	0.4	52.1	2.1	−1.3	17.3	4.5	*	***Na130-U***	**2.67**	***Na130-U***	2.67
Na***130***-1	2.4	0.5	53.9	2.2	−1.4	17.7	2.1	−2.3	Na***130***-P1	**2.68**	Na***130***-G1	2.67
Na***130***-2	2.4	0.5	53.6	2.1	−1.5	18.1	*	*		***(+0.02)***		***(+0.01)***
Na***130***-3	4.5	0.5	52.4	2.2	−1.4	17.7	4.0	−0.4			Na***130***-G2	2.67
Na***130***-4	6.0	0.4	51.2	2.1	−1.5	18.1	*	*	Na***130***-P2	**2.67**		***(+0.01)***
Na***130***-5	4.4	0.5	52.2	2.2	−1.4	17.7	*	*		***(+0.01)***		
Na***130***-6	6.1	0.4	51.0	2.1	−1.5	18.1	*	*			Na***130***-G3	2.65
Na***130***-7	5.9	0.4	51.5	2.1	−1.5	18.1	4.6	+0.2				***(-0.01)***
L***Na130-U***	4.8	0.4	52.4	2.1	−1.0	16.0	4.5	*	L***Na130-U***	**2.68**	L***Na130-U***	2.68
LNa***130***-1	2.0	0.4	52.3	2.1	−1.2	16.8	1.8	−2.6	LNa***130***-P1	**2.69**	LNa***130***-G1	2.69
LNa***130***-2	3.0	0.4	51.5	2.1	−1.4	17.7	*	*		***(+0.03)***		***(+0.03)***
LNa***130***-3	1.9	0.5	55.4	2.1	−1.4	17.7	2.1	−2.3			LNa***130***-G2	2.68
LNa***130***-4	2.9	0.4	53.8	2.1	−1.4	17.7	*	*	LNa***130***-P2	**2.68**		***(+0.02)***
LNa***130***-5	7.9	0.4	50.5	2.2	−1.3	17.3	*	*		***(+0.02)***		
LNa***130***-6	5.1	0.4	52.1	2.2	−1.3	17.3	*	*			LNa***130***-G3	2.68
LNa***130***-7	4.1	0.4	52.6	2.1	−1.3	17.3	3.8	−0.6				***(+0.02)***

(b) $MgCl_2$ flooded	SiO_2	MgO	CaO	$\delta^{13}C_{SMOW}$	$\delta^{18}O_{SMOW}$	T	SSA	ΔSSA	sample	ρ_{end}	sample	ρ_{end}
	(wt%)	(wt%)	(wt%)	(‰)	(‰)	(°)	m2/g	m2/g		g/cm3		g/cm3
Mg25-U	4.5	0.4	53.6	2.2	−0.9	15.6	4.3	*	Mg25-U	2.65	Mg25-U	2.65
Mg25-1	3.5	0.7	53.1	2.3	−1.1	16.3	6.1	+1.7	Mg25-P1	2.66	Mg25-G1	*
Mg25-2	3.5	0.5	53.2	2.1	−1.2	16.7	*	*		(0.00)		
Mg25-3	3.7	0.5	53.5	2.2	−0.9	15.7	4.5	+0.1			Mg25-G2	*
Mg25-4	3.8	0.5	53.1	2.3	−0.9	15.8	*	*	Mg25-P2	2.65		
Mg25-5	4.4	0.5	52.3	2.3	−1.0	16.1	*	*		(-0.01)		
Mg25-6	3.5	0.5	53.2	2.3	−1.0	16.0	*	*			Mg25-G3	*
Mg25-7	5.0	0.5	52.3	2.3	−1.0	16.1	3.9	−0.5				
Mg60-U	3.5	0.4	53.1	1.9	−1.3	17.3	3.7	*	Mg60-U	2.66	Mg60-U	2.66
Mg60-1	3.5	1.4	51.9	2.2	−0.8	15.2	6.7	+2.3	Mg60-P1	2.69	Mg60-G1	2.69
Mg60-2	3.7	0.7	52.7	2.2	−1.0	16.2	*	*		(+0.03)		(+0.03)
Mg60-3	4.6	0.6	52.5	2.3	−0.9	15.7	6.4	+2.0			Mg60-G2	2.68
Mg60-4	5.5	0.5	52.0	2.2	−1.0	16.1	*	*	Mg60-P2	2.69		(+0.02)
Mg60-5	3.6	0.5	53	2.1	−1.2	17.0	*	*		(+0.03)		
Mg60-6	3.4	0.5	53.1	2.1	−1.0	16.1	*	*			MgMg60-G3	2.69
Mg60-7	3.2	0.5	53.1	2.3	−1.0	16.2	3.6	−0.8				(+0.03)
Mg92-U	4.1	0.4	52.6	2.1	−1.3	17.3	4.8	*	Mg92-U	2.66	Mg92-U	2.66
Mg92-1	I.S.	I.S.	I.S.	2.2	−1.4	17.7	6.8	+2.4	Mg92-P1	2.69	Mg92-G1	2.7
Mg92-2	3.3	1.9	51.8	2.2	−1.2	16.8	*	*		(+0.03)		(+0.04)
Mg92-3	3.8	1.1	52.0	2.2	−1.3	17.3	4.5	+0.1			Mg92-G2	2.69
Mg92-4	3.6	1.0	52.0	2.2	−1.3	17.3	*	*	Mg92-P2	2.68		(+0.03)
Mg92-5	3.8	0.9	52.3	2.2	−1.3	17.3	*	*		(+0.02)		
Mg92-6	3.8	0.8	52.5	2.2	−1.2	16.8	*	*			Mg92-G3	2.68
Mg92-7	3.9	0.7	52.4	2.2	−1.2	16.8	3.9	−0.5				(+0.02)
Mg110-U	4.2	0.4	53.1	2.2	−0.9	15.6	4.8	*	Mg110-U	2.66	Mg110-U	2.66
Mg110-1	2.9	2.6	52.0	2.3	−1.4	17.5	6.8	+2.4	Mg110-P1	2.69	Mg110-G1	*
Mg110-2	3.7	2.4	51.7	2.3	−1.1	16.2	*	*		(+0.03)		
Mg110-3	3.5	2.2	52.2	2.2	−1.0	16.2	7.9	+3.5			Mg110-G2	*
Mg110-4	3.6	2.0	52.1	2.3	−1.1	16.3	*	*	Mg110-P2	2.69		
Mg110-5	3.0	1.6	52.8	2.3	−0.9	15.6	*	*		(+0.03)		
Mg110-6	3.8	1.0	52.8	2.3	−1.0	16.0	4.8	+0.4			Mg110-G3	*
Mg130-U	4.0	0.4	53.0	2.1	−1.1	16.4	3.8	*	Mg130-U	2.67	Mg130-U	2.67
Mg130-1	3.8	3.2	50.2	2.2	−1.3	17.3	6.7	+2.3	Mg130-P1	2.70	Mg130-G1	2.69
Mg130-2	4.1	3.6	49.4	2.2	−1.2	16.8	*	*		(+0.04)		(+0.03)
Mg130-3	3.7	3.3	50.0	2.2	−1.3	17.3	7.8	+3.4			Mg130-G2	2.69
Mg130-4	4.3	2.8	50.3	2.2	−1.2	16.8	*	*	Mg130-P2	2.70		(+0.03)
Mg130-5	5.3	2.9	49.5	2.2	−1.2	16.8	*	*		(+0.04)		
Mg130-6	5.2	2.6	49.7	2.2	−1.1	16.4	*	*			Mg130-G3	2.68
Mg130-7	6.2	2.6	49.3	2.3	−0.9	15.6	9.0	+4.6				(+0.02)
LMg130-U	6.0	0.4	51.5	2.2	−1.6	18.5	4.9	*	LMg130-U	2.67	LMg130-U	2.67

(*continued on next page*)

Table 3 (*continued*)

(b) $MgCl_2$ flooded	SiO_2	MgO	CaO	$\delta^{13}C_{SMOW}$	$\delta^{18}O_{SMOW}$	T	SSA	ΔSSA	sample	ρ_{end}	sample	ρ_{end}
	(wt%)	(wt%)	(wt%)	(‰)	(‰)	(°)	m2/g	m2/g		g/cm3		g/cm3
LMg130-1	4.0	5.7	46.8	1.5	−3.0	24.8	6.8	+2.4	LMg130-P1	2.71	LMg130-G1	2.72
LMg130-2	4.4	7.5	44.5	1.9	−2.9	24.3	*	*		(+0.05)		(+0.06)
LMg130-3	7.3	5.2	46.0	2.0	−2.2	21.2	7.7	+3.3			LMg130-G2	2.69
LMg130-4	3.9	3.2	50.0	2.0	−2.0	20.3	*	*	LMg130-P2	2.69		(+0.03)
LMg130-5	3.8	2.4	51.1	2.0	−1.7	19.0	*	*		(+0.03)		
LMg130-6	I.S.	I.S.	I.S.	2.0	−1.7	19.0	*	*			LMg130-G3	2.69
LMg130-7	4.1	2.4	51.1	1.7	−1.9	19.8	5.7	+1.3				(+0.03)

volume has remained constant during the compaction process.

Estimates of the *true* porosity, i.e. the ratio of pore volume and bulk volume after flooding-compaction tests must necessarily account for all volume changes. This is found by direct measurement using end state properties only.

One such estimate is made using the difference between the saturated and dry weights ($M_{sat,end}$ and $M_{dry,end}$) divided by the density of distilled water (ρ_{dw}) and the bulk volume ($V_{b,end}$, which is given by Eq. (3)):

$$\phi_{end,2} = \frac{(M_{sat,end} - M_{dry,end})}{\rho_{dw} V_{b,end}} \tag{7}$$

just as for the evaluation of the initial porosity, see Eq. (1).

The true porosity can also be estimated by combining the solid density ($\rho_{s,end}$), the dry mass ($M_{dry,end}$) and bulk volume ($V_{b,end}$) after the experiment as:

$$\phi_{end,3} = \frac{V_p}{V_b} = 1 - \frac{V_s}{V_b} = 1 - \frac{M_{dry,end}}{V_{b,end}\rho_{s,end}} \tag{8}$$

Here, the solid density ($\rho_{s,end}$) is the weighted average ($\rho_{core,avg}$) from parts P1 and P2, listed in Table 3 (see 2.9. ***Solid density estimation***).

2.12. Permeability estimation

From the differential pressure (ΔP) across the core plug and with known flooding volumetric rate (Q), the permeability during testing (k) was calculated according to Darcy's equation:

$$k = \frac{Q \cdot \mu \cdot L}{\Delta P \cdot A} \tag{9}$$

where L is the length of the core, A is the cross-sectional area, and μ is the brine viscosity, varying with temperature (Crittenden et al., 2012).

3. Results

3.1. Field emission gun-scanning electron microscopy (FEG-SEM)

3.1.1. Unflooded samples

Aalborg chalk can be classified as a coccolithophore-containing mudstone or wackestone with high abundance of foraminifer shells and fragments of a variety of shells. Well-preserved coccolithophore plates (coccoliths) are present (Fig. 2a, c, pink arrows), but commonly show some overgrowth. However, the matrix is dominated by small calcite grains, originating most likely from broken coccolithophore species and foraminifera shells. Intra-fossil porosity is partly preserved. This chalk contains large amounts of authigenic opal-CT lepispheres (Fig. 2a, c, yellow squares). In cases, opal-CT fills entire foraminifer shells. Flake shaped clay minerals are observed (Fig. 2a, c, green circles), some of which might be mica as also documented by Hjuler (2007). In addition, large elongated pores are found, interpreted to be sponge spicule moulds (Fig. 2b, light orange dotted circle).

3.1.2. NaCl flooded samples

In both cores (***Na130*** and L***Na130***) flooded with NaCl at 130 °C, inorganic calcite together with preserved coccolithophores (Fig. 3a, b, c pink arrows) and clay minerals (Fig. 3a, green circles) can still be found, similar to observations in unflooded Aalborg chalk (Fig. 2). FEG-SEM images of each slice from ***Na130*** and L***Na130*** are documented in supplementary material (sup. mat. Figs. 1 and 2). There is no indication of newly-formed minerals, in agreement with former studies (Andersen et al., 2017; Madland et al., 2011; Megawati et al., 2015; Wang et al., 2016). The calcite grains appear, however, somewhat more rounded (Fig. 3a and b) compared to unflooded material (Fig. 2). This might be linked to the slight dissolution of calcite also indicated in effluent measurements (see below). Unbroken microfossils besides coccolithophores can still be observed in the cores.

In ***Na130***, opal-CT cannot be found in slice 1 in areas imaged by FEG-SEM (sup. mat. Fig. 1a), but partly preserved opal-CT in slice 2 (sup. mat. Fig. 1b) can be observed. In slice 3 (sup. mat. Figs. 1c) and 4 (sup. mat. Fig. 1d) of the core, partly dissolved and/or dismantled opal-CT can still be found, and in slice 4 large pores filled with opal-CT are present, as in unflooded material. From approximately slice 5 (sup. mat. Fig. 1e) along the flooding axis until the outlet (Fig. 1), opal-CT seems preserved. Near the outlet part of the core, small flakes of clay-like minerals can be observed (Fig. 3a green circle in slice 7).

In L***Na130***, within slice 1 (sup. mat. Fig. 2a), partly preserved opal-CT is infrequently observed (Fig. 3b and c, yellow squares), which is different from slice 1 in ***Na130***, however, in most areas of this sample, opal-CT cannot be found. In all slices towards the outlet of the core (sup. mat. Fig. 2g), a trend from partly preserved opal-CT towards well-preserved opal-CT is observed. In slice 6 large pore spaces can be observed filled with opal-CT (Fig. 3c, yellow squares), similar as in unflooded material. Unbroken microfossil shells are still observed in all slices.

3.1.3. $MgCl_2$ flooded samples

FEG-SEM images from $MgCl_2$ flooded cores under different temperatures are shown in Fig. 4 and sup. mat. Figs. 3–8. In the cores flooded with $MgCl_2$ organic and inorganic calcite is still present along with occurrences of flake shaped clay minerals and quartz. The calcite grains in all samples appear more rounded (Fig. 4a and b), indicative of dissolution, but unbroken microfossil shells and coccolithophores can still be observed.

The two cores, L***Mg130*** and ***Mg130***, tested at 130 °C, definitely show the strongest mineralogical changes. Magnesite crystals are observed from the inlet along the flooding direction (Fig. 1) until slice 4 (Fig. 4d). Large magnesite crystals, typically between 1 and 6 µm, are found in open pore spaces, mostly inside foraminifera shells (Fig. 4c). In addition, smaller crystals (~50–100 nm) in clusters with high content of magnesium are observed at the inlet of the cores flooded with $MgCl_2$ at 130 °C (Fig. 4d), which also are interpreted to be newly grown magnesite. Such observations of smaller magnesite crystals grown in aggregates inside pore spaces are found throughout both cores flooded at 130 °C (Fig. 4e). In the cores tested at 25, 60, 92 and 110 °C, magnesite crystals are not observed (sup. mat. Figs. 3–6), however in core

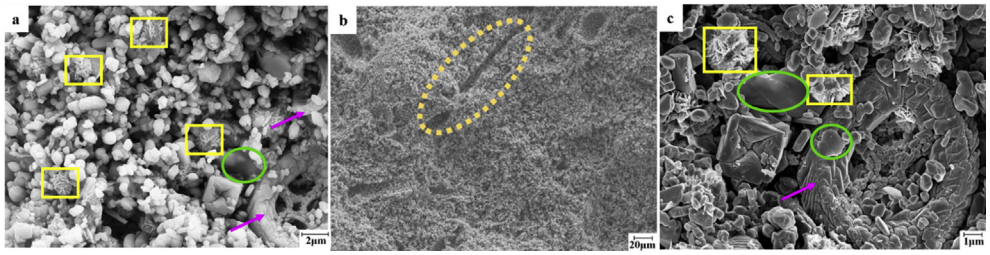

Fig. 2. FEG-SEM images of unflooded Aalborg cores. (a) Opal-CT and coccolithophores are widespread in unflooded material; (b) Sponge spicule moulds are observed in unflooded Aalborg chalk; (c) SEM-micrograph of unflooded Aalborg chalk. Along with microfossils such as coccoliths, intact and dismantled, clay minerals and phyllosilicates can be observed. Yellow square: opal-CT; pink arrow: coccoliths; green circle: clay minerals; orange dotted line: sponge spicule mould. (For interpretation of the references to colour in this figure legend, the reader is referred to the Web version of this article.)

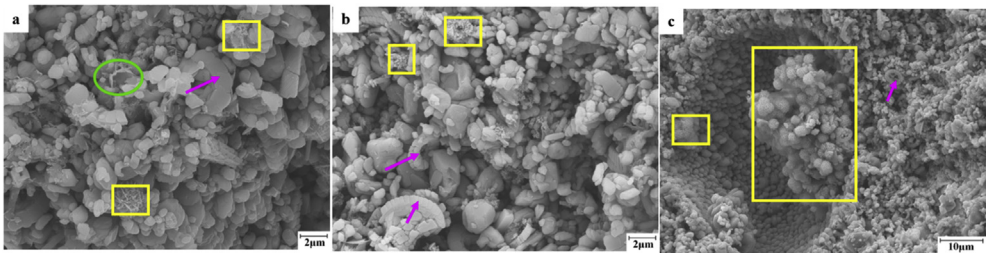

Fig. 3. (A) Clay-minerals, preserved opal-CT and coccolithophores in the Na***130*** (slice 7); (b) SEM-micrograph of NaCl-flooded L***Na130*** (slice 2). Partly preserved opal-CT (yellow square) are widespread. (c) Large cluster of opal-CT found inside foraminifera shells in LNa***130*** (slice 6). Yellow square: opal-CT; pink arrow: coccoliths; green circle: clay minerals. (For interpretation of the references to colour in this figure legend, the reader is referred to the Web version of this article.)

Mg92 (flooded with $MgCl_2$ at 92 °C) small crystals less than 100 nm in size are observed on surface of larger calcite grains (Fig. 4b, blue circle).

Opal-CT can still be found in all cores flooded with $MgCl_2$. However, the lepispheres have different morphology depending on which temperature the cores were flooded at. Samples ***Mg25*** and ***Mg60*** (Fig. 4h) contain minute amount of Si-Mg-bearing precipitates near the inlet according to FEG-SEM-EDS, while well preserved opal-CT is widespread from slice 2 (sup. mat. Figs. 3b and 4b) up to the outlet of the cores (Fig. 4a, yellow square). For the core flooded at 92 °C clay-minerals are found from the inlet until slice 5 (sup. mat. Fig. 5e) in the core, while in slice 6 (sup. mat. Figs. 5f) and 7 (sup. mat. Fig. 5g) the flooded material again appears quite similar to the unflooded rock. In core ***Mg110*** newly formed Si-Mg-bearing minerals are observed from slice 1 (sup. mat. Fig. 6a) towards the outlet (sup. mat. Fig. 6g). In the high-temperature tested cores (***Mg130*** and L***Mg130***), minute opal-CTs can still be found at the inlet of the cores, but their texture and composition are changed (Fig. 4f, blue dotted arrow) as follows: the blades in the lepispheres are partly dissolved and smaller, and connected in a film-like manner. From slice 2 (sup. mat. Figs. 7b and 8b) up to the outlet (sup. mat. Figs. 7g and 8g), opal-CT can no longer be observed, but instead Si-Mg-bearing minerals are abundant throughout the two cores flooded at 130 °C (Fig. 4g, pink dotted square), as also seen in ***Mg110***. An increase of Si-Mg-bearing minerals content towards the outlet of the cores is observed.

As described (above 2. ***Experimental procedures and methods***), the effluent was collected during all tests. White particles have been suspended in the effluent produced by core L***Mg130***, which was not observed in other tests. These effluent samples were filtered and dried at 100 °C in a heating chamber before analysed by FEG-SEM-EDS. Fig. 4i and l shows the FEG-SEM-EDS analysis of the white particles. The particles are SiO_2-bearing minerals, precipitated from the fluid saturated with Si^{4+} through dissolution in core L***Mg130***.

3.2. X-Ray Diffraction (XRD)

3.2.1. Unflooded samples

The minerology of Aalborg chalk, the clastic and the < 2 μm fractions of the chalk were determined by XRD on representative samples (sup. mat. Fig. 9a) (Bertolino et al., 2013). The unflooded Aalborg chalk contains calcite and non-carbonate phases, which are composed of scarce quartz, scarce phyllosilicates (broad peak at 4.44 – 4.50 Å) and traces of opal-CT (two broad reflections at 4.32 Å and 4.09 Å) (Wilson, 2014), minor clinoptilolite and scarce illite and illite/smectite.

3.2.2. NaCl flooded samples

The NaCl flooded cores do not show any new minerals, in agreement with previous studies (Madland et al., 2011; Megawati et al., 2015). Both NaCl flooded cores (***Na130*** and L***Na130***, sup. mat. Fig. 9b and c) contain calcite as the dominant mineral, along with scarce quartz, scarce phyllosilicates and traces of opal-CT, also found in unflooded material. In ***Na130*** quartz and opal-CT are observed in all slices. Clay minerals are recognized only in slice 7. L***Na130*** differs slightly from ***Na130***. As in ***Na130,*** scarce quartz is distributed in all slices of L***Na130***, however, traces of opal-CT can only be found from slice 5 on and increases from slice 5 to 7 along with scarce clay minerals.

3.2.3. $MgCl_2$ flooded samples

XRD analyses of $MgCl_2$ flooded cores are shown in sup. mat. Fig. 9d–i. All $MgCl_2$ flooded cores still contain calcite as the dominant mineral, along with minor quartz, and scarce phyllosilicates, which were also found in unflooded material. In ***Mg25*** opal-CT was detected from inlet to the outlet while in ***Mg60*** opal-CT was absent in slice 1 (sup. mat. Fig. 9d and e), but present from slice 2 to 7. Opal-CT is concentrated mainly in slice 4 to 6 in core ***Mg92*** and opal-CT was not found in cores ***Mg110, Mg130*** *and* L***Mg130*** (sup. mat. Fig. 9f, g, h, i). Traces of magnesite were detected in slice 4 of ***Mg110*** (110 °C), and the cores tested at 130 °C (***Mg130*** *and* L***Mg130***) show well-developed peaks of magnesite at 2.74 – 2.76 Å in slices 1–4.

3.3. Whole-rock geochemistry

Geochemical analyses of the unflooded chalk are summarized in Table 3 (complete data set is in sup. mat. Table 1) together with the exact sample position of the unflooded samples.

3.3.1. Unflooded samples

Calcite is the dominant mineral and CaO ranges from 51.4 to 53.6 wt% (weight percentage). Al_2O_3 and MgO contents are low, 0.34 and 0.40 wt%, respectively, with total carbon (TOC) around 12%. SiO_2 appears in concentrations between 3.5 wt% and 6.0 wt% and is mainly present as opal-CT, according to FEG-SEM and XRD studies. Opal-CT

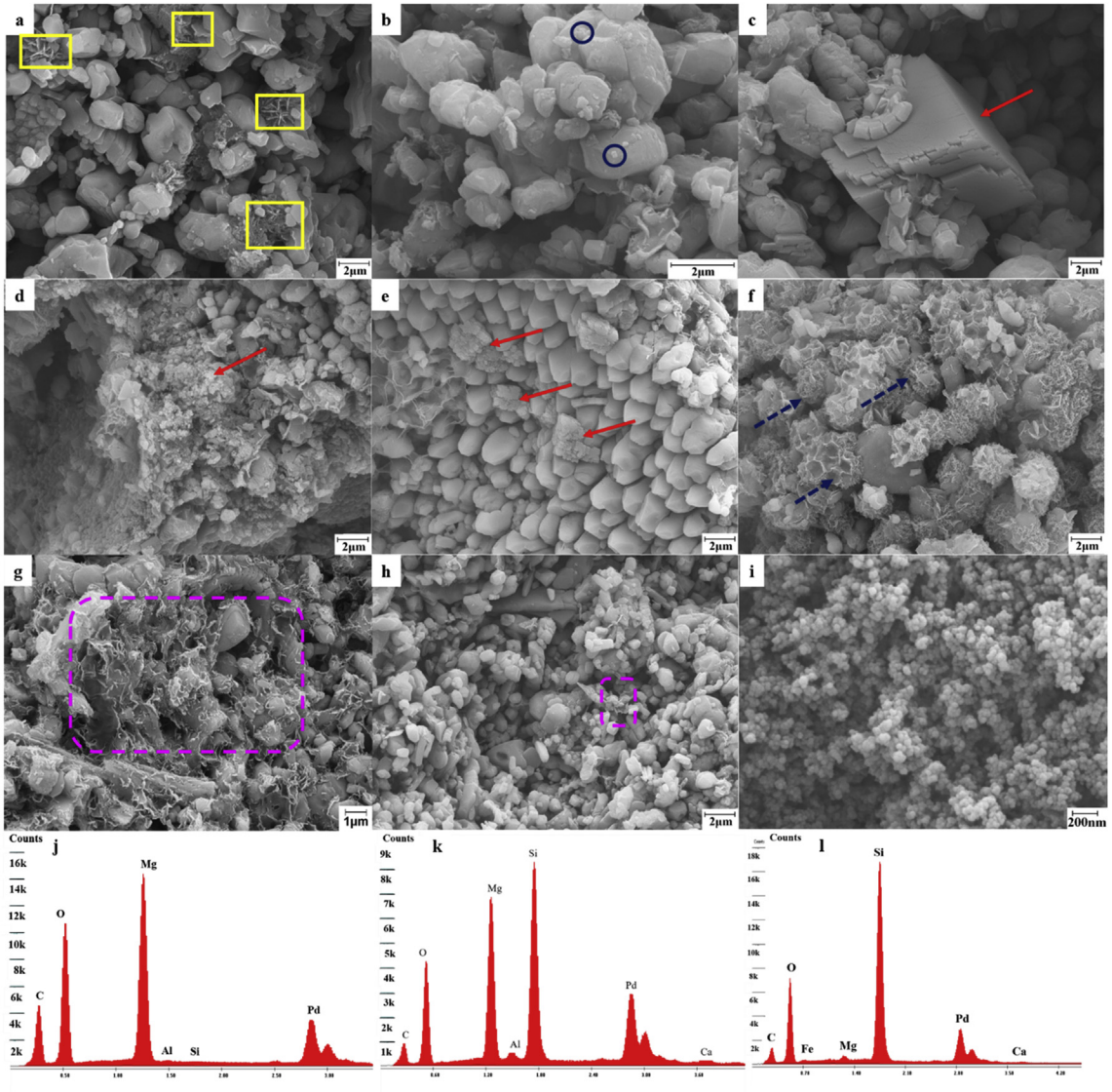

Fig. 4. (A) The calcite grains seem more rounded after flooding (*Mg**60***, slice 5). Opal-CT is widespread; (b) Small crystals on top of calcite grains found in *Mg**92*** (slice 1). These are similar to high Mg-content grains observed in chalk flooded with $MgCl_2$ at 130 °C; (c) Magnesite in L*Mg**130*** (slice 1); (d) Smaller grains with high magnesium content, interpreted to be new-grown magnesite from L*Mg**130*** (slice 1); (e) Aggregates of magnesite crystals in core *Mg**130*** (slice 5); (f) Remnants of opal-CT lepispheres with changed texture and composition from L*Mg**130***, slice 1; (g) Si-Mg-bearing minerals are widespread in *Mg**130***, slice 7; (h) Minute Si-Mg-bearing minerals are observed in *Mg**60***, slice 1; (i) SEM image of white particles found in the effluent of L*Mg**130*** flooding test; (l) EDS analysis of the large crystal in the centre of c (k) EDS analysis of the altered opal-CT in f (l) EDS analysis (identified as SiO_2) of the white particles found in the effluent of L*Mg**130*** flooding test (sample coated with palladium, Pd, for sufficient electron flux). Red arrow: magnesite; yellow square: opal-CT; pink dotted square: Si-Mg-bearing minerals; blue dotted arrow: changed opal-CT; blue circle: high magnesium content particles. (For interpretation of the references to colour in this figure legend, the reader is referred to the Web version of this article.)

constitutes the main non-carbonate mineral. Sr abundance varies between 692 and 881 ppm but does not correlate positively with CaO. Trace element geochemistry does not point to any significant clastic input. Rb and Y, with values far below 5 and 6 ppm respectively, are even below 10% of the typical upper continental crust composition (McLennan et al., 2006).

3.3.2. *NaCl flooded samples*

Compared to unflooded material; in the NaCl flooded cores the whole-rock geochemical analyses show significant changes only for SiO_2 (Table 3a and sup. mat. Table 1). In *Na**130***, SiO_2 increases from low values at the inlet (2.4 wt%) towards higher at the outlet (5.9 wt%). The values at the inlet are 50% lower than in the unflooded sample and at the outlet approximately 20% higher than in unflooded chalk in this study (Table 3a and sup. mat. Table 1). The same trend can be observed in L*Na**130***. Highly fluid-sensitive Sr and TOC are constant. The content of major elements (Mg, Al, Na and K) varies slightly along the cores, however this is not possible to interpret as other than natural variation and the initial low abundance being the dominant factors, rather than effects of flooding.

3.3.3. *$MgCl_2$ flooded samples*

The whole-rock geochemistry analysis of $MgCl_2$ flooded cores is summarized in Table 3b. The flooded cores display in general an increase in MgO and a decrease in CaO and SiO_2, although trends are by far more complex dependent on temperature. The MgO enrichment increases with increasing temperatures. All the unflooded cores had similar very low concentrations of MgO (0.4 wt%), but obtained different enrichments of MgO after flooding. The cores flooded at lower temperatures (25, 60, 92 and 110 °C) show decreasing trends of MgO

content from the inlet to the outlet, with the most significant increase of MgO near the inlet (Table 3b). In ***Mg130*** and L***Mg130*** the MgO-concentrations showed similar decreasing trends, however with the highest content in slice 2 (***Mg130***: 3.6 wt%; ***Mg130***: 7.5 wt%), and then decreasing towards the outlet slice (***Mg130***: 2.6 wt%; ***Mg130***: 2.4 wt%). ***Mg130*** obtained less MgO enrichment (on average: 3.0 wt%, 61 days) than L***Mg130*** (on average: 4.4 wt%, 115 days) as expected with the shorter flooding time.

In core ***Mg25*** the amount of SiO_2 increases from inlet (3.5 wt%) to outlet (5 wt%). ***Mg92, Mg110*** and ***Mg130*** show similar trends as ***Mg25***. The long-time flooded core L***Mg130*** shows a rather uniform SiO_2-distribution besides in slice 3, with enriched abundances (22% higher) compared to the unflooded sample. ***Mg60*** shows constant SiO_2-concentrations with an enrichment in slices 3 and 4. It should be noted that the SIO_2-content in the flooded cores may also be influenced by natural SiO_2-variations (varying between 3.5 and 6.0 wt% in unflooded material, sup. mat. Table 1a), mainly linked to the abundance of opal-CT. Flooding did not measurably affect the concentrations of Al_2O_3, Fe_2O_3, K_2O and TOC (Table 3b).

3.4. Stable isotope geochemistry

3.4.1. Unflooded samples

C-O isotope measurements are summarized in Table 3. For unflooded material, the $\delta^{13}C_{SMOW}$ values are homogeneous, varying between 2.0 and 2.3‰, besides one value of 1.9‰ in sample ***Mg60-U*** (sup. mat. Table 1a). $\delta^{18}O_{SMOW}$ values vary more strongly, between −0.9 and −1.6‰ (sup. mat. Table 1a). However, both isotope proxies still reflect primary signatures in accordance to earlier studies (Surlyk et al., 2010). Facies differences in chalk through time of deposition of the Rørdal Member were observed by Surlyk et al. (2010) and expressed with a trend from lighter to heavier isotopes for $\delta^{18}O_{SMOW}$, hence from warmer to colder environment stratigraphically towards younger rocks. If applying this trend as criteria for a stratigraphic position for the samples studied here (and explaining value differences) L***Mg130-U***, AA2-***U***, ***Na130-U*** and ***Mg92-U*** are from the bottom of the member and the others rather from the top with ***Mg110-U,*** AA7-U and AA4-U being the youngest (sup. mat. Table 1a) of the cores.

3.4.2. NaCl flooded samples

$\delta^{13}C_{SMOW}$ values in the NaCl flooded cores (Table 3a) are comparable to those of unflooded cores. In contrast, $\delta^{18}O_{SMOW}$ values for L***Na130*** are over 30% more negative than in the unflooded sample, uniformly throughout the core. The difference before and after flooding within sample ***Na130*** is less, which was flooded only 60 days compared to 118 days for L***Na130***. Nevertheless, both samples are still in vicinity of the expected isotope range for the Rørdal Member (Surlyk et al., 2010), but the altered values could indicate a reactivity to the flooding process.

Table 4
Core properties (yield point and bulk modulus) during hydrostatic loading and confining pressure during creep.

Core	Yield point	Bulk modulus	Confining pressure during creep
	(MPa)	(GPa)	(MPa)
Mg25	8.23	0.30	10
Mg60	7.23	0.21	10
Mg92	8.86	0.31	11
Mg110	4.39	0.29	8
Mg130	8.41	0.23	11
L***Mg130***	8.48	0.24	11
Na130	8.77	0.28	12
L***Na130***	8.92	0.23	12

3.4.3. $MgCl_2$ flooded samples

After $MgCl_2$ flooding, the average $\delta^{13}C_{SMOW}$ values (Table 3b) are mostly similar to those of the unflooded cores with few exceptions. This may reflect natural variation rather than effects of the flooding experiments. $\delta^{18}O_{SMOW}$ values vary, but generally reflect Cretaceous values (Surlyk et al., 2010). Sample ***Mg25***, shows more negative values in slice 1 and 2, the other slices are comparable to unflooded values. ***Mg60*** and ***Mg92*** contain values which match the unflooded samples, while ***Mg110*** and ***Mg130*** have slightly more negative values in the first two and three slices, respectively, and then show similar values to those of the unflooded samples. Only L***Mg130*** is different with strongly more negative values throughout the entire sample, with the most negative values in slice 1 and 2.

3.5. Mechanical tests-hydrostatic loading and creep compaction

The measured axial stress *versus* axial strain during loading phase is plotted in Fig. 5a. Yield points, bulk modulus and confining pressure during the creep phase are reported in Table 4. The cores flooded at the same temperature and same fluid show similar yield point and bulk modulus (see Table 4). Concerning yield point and bulk modulus no direct trend due to temperature, nor injected brines, could be drawn, which is consistent with previous observation (Madland et al., 2011; Megawati et al., 2015; Wang et al., 2016).

During the creep phase, the impacts of both brines and the flooding temperatures are clearly demonstrated in the axial creep strain profiles, see Fig. 5b. Cores, flooded at the same temperature and with the same fluids (***Na130*** and L***Na130***; L***Mg130*** and ***Mg130***), showed good repeatability. Longer flooding time led to more creep compaction with the same brine injection at 130 °C (L***Mg130***: 6.51% and ***Mg130***: 5.36%; L***Na130***: 2.41% and ***Na130***: 1.60%) and $MgCl_2$-flooded cores compacted more than NaCl-flooded cores at 130 °C, similar to previous studies (Madland et al., 2011; Megawati et al., 2015; Wang et al., 2016). As Fig. 5b shows, after 60 days of creep, all $MgCl_2$-flooded cores

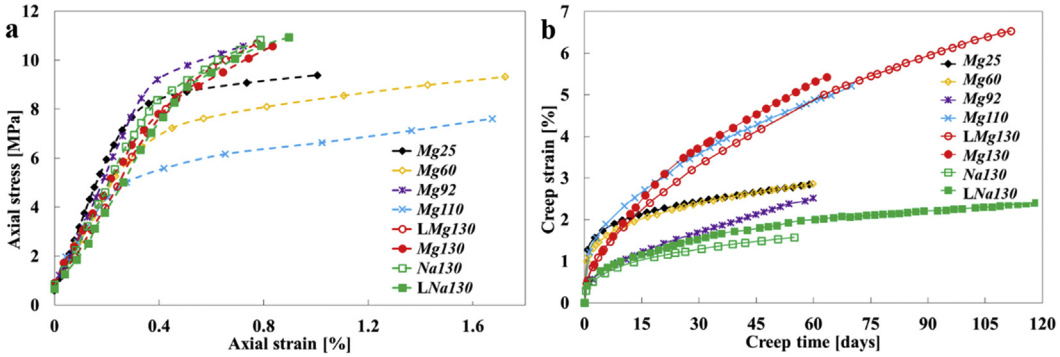

Fig. 5. (A) Axial stress versus axial strain for $MgCl_2$ or NaCl flooded cores; (b) axial creep strain versus creep time during $MgCl_2$ or NaCl flooding. Note that L***Mg130*** and L***Na130*** were flooded for 115 and 118 days respectively.

in the temperature range from 25 to 110 °C compacted more than the NaCl-flooded cores at 130 °C.

We divided the creep behaviour of $MgCl_2$-and NaCl-flooded cores into two phases. During the primary phase (the first ~ 10 days), cores ***Mg25***, ***Mg60***, ***Mg110*** showed higher creep rates than other cores ***Mg92***, ***Mg130***, L***Mg130***, L***Na130*** and ***Na130*** due to higher compaction rates at the end of the hydrostatic loading and thereby entering the creep phase at higher strain rates. The remaining part of the creep phase, where loading phase effects are assumed negligible, is defined as the secondary phase. During this part of the test, systematically higher creep rates (axial creep strain divided by creep time) were observed at higher temperatures for $MgCl_2$-flooded cores (***Mg25***: 0.015%/day; ***Mg60***: 0.015%/day; ***Mg92***: 0.029%/day; ***Mg110***: 0.039%/day; L***Mg130***: 0.045%/day; ***Mg130***: 0.052%/day). Cores ***Mg25*** and ***Mg60*** had similar low compaction rates as the NaCl flooded cores from 20 until 60 days of creep (Fig. 5b, black and green curves, L***Na130***: 0.013%/day; ***Na130***: 0.013%/day).

3.6. Effluent analyses

During NaCl flooding the effluent concentrations of Na^+ and Cl^- are practically the same as the injected (not shown), i.e. 0.657 mol/L, and only minute Ca^{2+} concentrations are observed (Fig. 6a), in line with previous studies (Andersen et al., 2017; Madland et al., 2011; Megawati et al., 2015; Wang et al., 2016). Fig. 6a, b and c show the measured Ca^{2+}, Mg^{2+} and Si^{4+} concentration profiles with time during flooding, respectively. As temperature increases, more Ca^{2+} is produced and more Mg^{2+} is retained inside the cores (Fig. 6a and b), which is expected based upon findings from a previous studies (Korsnes et al., 2006a; Nermoen et al., 2016). Ca^{2+} production in ***Mg25*** (~0.003 mol/L) is comparable to that of the two NaCl flooded cores (L***Na130***: ~0.002 mol/L; ***Na130***: ~0.003 mol/L), and is slightly lower than ***Mg60*** (~0.007 mol/L). All cores show Ca^{2+} peaks initially (Fig. 6a) followed by a slightly decreasing trend until the concentrations stabilize (Fig. 6a, Ca^{2+} concentration: L***Na130***: ~0.002 mol/L; ***Na130***: ~0.003 mol/L; ***Mg25***: ~0.003 mol/L; ***Mg60***: ~0.007 mol/L ***Mg92***: ~0.010 mol/L; ***Mg110***: ~0.014 mol/L; L***Mg130***: ~0.016 mol/L; ***Mg130***: ~0.023 mol/L). In the cores flooded with $MgCl_2$ at high temperatures (110 and 130 °C), a clear decrease in Ca^{2+} concentrations is observed and negatively correlated with Mg^{2+} concentrations from the same cores. In all other cores, the production of Ca^{2+} is rather stable over time.

Fig. 6b shows the Mg^{2+} concentration in the effluent of the $MgCl_2$ flooded cores. The trends are similar but opposite to the Ca^{2+} profiles, i.e. the sum of produced Ca^{2+} and Mg^{2+} was stable and close to equal to the injected concentration of 0.219 mol/L (not shown), consistent with earlier studies (Andersen et al., 2017; Madland et al., 2011; Megawati et al., 2015; Wang et al., 2016). The Mg^{2+} concentration in the effluent of tests from ***Mg25*** (~0.22 mol/L) and ***Mg60*** (~0.22 mol/L) were almost stable over the entire test period. For ***Mg92***, ***Mg110***, L***Mg130*** and ***Mg130*** the magnesium concentration increased from low values in the first sample points (***Mg92***: 0.198 mol/L; ***Mg110***: 0.196 mol/L; L***Mg130***: 0.167 mol/L; ***Mg130***: 0.175 mol/L), until they stabilized (Fig. 6b, Mg^{2+} concentration: ***Mg92***: ~0.21 mol/L; ***Mg110***: ~0.21 mol/L; L***Mg130***: ~0.20 mol/L; ***Mg130***: ~0.20 mol/L).

Concentrations of Si^{4+} were detected in the effluent (Fig. 6c), indicating dissolution of Si-bearing minerals. For a given core the Si^{4+} concentration was stable over time. ***Na130*** (~0.0012 mol/L) and ***Mg60*** (~0.0012 mol/L) produced similar amounts, which is a factor 2 higher than ***Mg25***. Highest Si^{4+} concentration has been observed in the effluent from the core ***Mg92*** (~0.0019 mol/L) and ***Mg110*** (~0.0019 mol/L), while the two cores tested at 130 °C (***Mg130***: ~0.0014 mol/L; L***Mg130***: ~0.0013 mol/L) produced less Si^{4+} than the two mentioned cores (***Mg92*** and ***Mg110***). For all effluent analyses, fluctuations may occur due to possible evaporation during storage and dilution uncertainties.

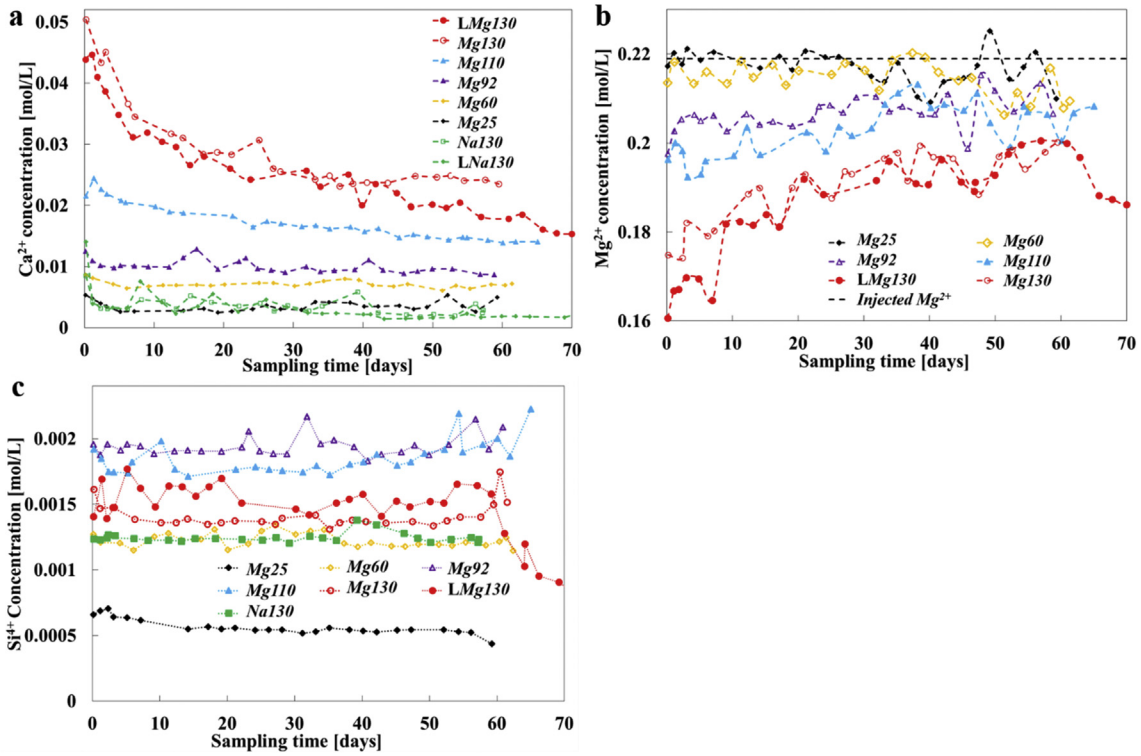

Fig. 6. Ion concentrations in the effluent samples measured by ion chromatography (a) Ca^{2+}concentration over time; (b) Mg^{2+} concentration over time; (c) Si^{4+} concentration measured by inductively coupled plasma. Note: Sample (L***Na130***) was not measured due to machine malfunction. Sampling times for ions (Ca^{2+}, Mg^{2+}, and Si^{4+}) were initiated at the start of the creep phases.

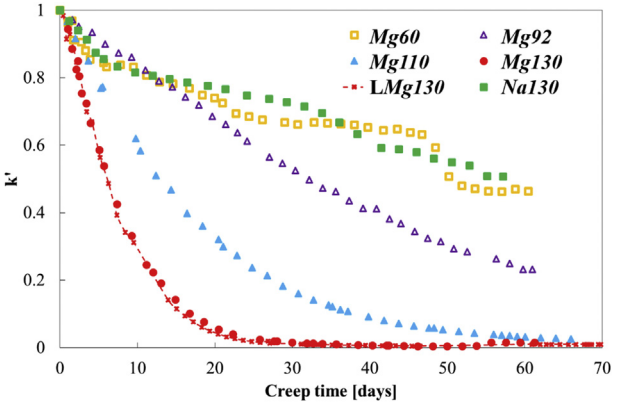

Fig. 7. Normalized permeability values (k' = k/k_ref) with creep time. In this figure, two cores (L*Na130* and *Mg25*) are not included due to fluctuations of the permeability values related to issues with the backpressure-regulator.

3.7. Solid density estimation

Table 3A, b shows the density values (ρ_{end}) from parts P1 and P2 and groups G1, G2 and G3 (see Fig. 1b) together with the calculated difference ($\Delta\rho$) between the end measurement (ρ_{end}) and the average pycnometry measurements (ρ_o) (2.66 g/cm^3) of unflooded material.

For the two NaCl flooded cores, $\Delta\rho$ (by group) was in the range between −0.01 and + 0.03 g/cm^3, where the increase is seen in the first group (*Na130*: G1: +0.01 g/cm^3 and L*Na130:* G1: +0.03 g/cm^3) with a decreasing trend towards the outlet of each core (*Na130*: G3: −0.01 g/cm^3 and L*Na130:* G3: +0.02 g/cm^3). This may be explained by a higher dissolution of opal-CT near the inlet and possible transported or precipitated lighter phases at the outlet.

For the $MgCl_2$ flooded cores, the density increase of P1 and P2 varied from zero to +0.05 g/cm^3 except for *Mg25*, which saw a small decrease in P2 (−0.01 g/cm^3) (Table 3b). Compared to the NaCl flooded cores the solid density increased more in the cores flooded with $MgCl_2$ at 130 °C, as observed in Wang et al. (2016). *Mg110* shows an increase in solid density in both P1 and P2 of 0.03 g/cm^3. Also by group measurements (G1, G2, G3), not performed on *Mg25* and *Mg110*, the $MgCl_2$ flooded cores showed the highest increase in solid density near the inlet (G1). L*Mg130* shows the highest increase near the inlet (G1: +0.06 g/cm^3), while a lower increase towards the outlet is observed (G2: +0.03 g/cm^3; G3: +0.03 g/cm^3). *Mg60*, *Mg92* and *Mg130* revealed similar trends as L*Mg130,* but in these cores the increase of the values is less (*Mg60*, G1: +0.03 g/cm^3, G3: +0.03 g/cm^3; *Mg92*, G1: +0.04 g/cm^3, G3: +0.02 g/cm^3; *Mg130*, G1: +0.03 g/cm^3, G3: +0.02 g/cm^3) than in L*Mg130*.

3.8. Specific surface area (SSA)

Measurements of the specific surface area (SSA) in slices 1, 3 and 7 of all flooded cores are listed in Table 3a and b together with the difference (ΔSSA) between measurements of material from the flooded cores and unflooded material (Table 1, average value unflooded: 4.4 m^2/g).

The SSA in the two NaCl flooded cores is decreased compared to the unflooded material measurement. The strongest decrease is observed near the inlet (*Na130*: −2.3 m^2/g; L*Na130*: −2.6 m^2/g) (Table 3a) while at the outlet, the measured values are (*Na130*: 4.6 m^2/g; L*Na130*: 3.8 m^2/g) close to the average value for unflooded material (4.4 m^2/g). The SSA values in the long-time (118 days) flooded core L*Na130* are lower than those of the short-time test (60 days) core *Na130*.

In *Mg25*, the SSA is increased in the first slice (+1.8 m^2/g) compared to the unflooded material (4.4 m^2/g). In the centre of the core (slice 3) there is only a slight increase (+0.1 m^2/g) while at the outlet (slice 7) the SSA has decreased to 3.9 m^2/g (−0.5 m^2/g compared to the average unflooded value). Only the significant increase in slice 1 can be considered an impact of the flooding process, while the other deviations are low enough to be within the natural variation of the rock (between 3.7 and 4.9 m^2/g, see Table 1).

Mg60 follows the same trend as *Mg25*, with a significant increase in the inlet slice (+2.3 m^2/g to 6.7 m^2/g) compared to the average value for unflooded material. However, in this core a considerable increase in SSA can also be found in slice 3 (+2.0 m^2/g), followed by a value of 3.6 m^2/g (−0.8 m^2/g) in slice 7. It should, however, be noted that the SSA for unflooded material from this particular core has been measured to 3.7 m^2/g and that local variation may impact the difference in measured SSA.

In the core flooded at 92 °C, *Mg92*, the initial SSA was higher, 4.8 m^2/g, and the SSA measured after flooding is increased at the inlet (slice 1: +2.4 m^2/g to 6.8 m^2/g compared to the average of unflooded material), while remained at approximately the initial value in slice 3 (−0.2 m^2/g). At the outlet, the value decreased to 3.9 m^2/g, much lower than both the average of unflooded material and the unflooded value for this specific core. However, the value is still within the range of natural variation in the core-samples of this study (Table 1).

Mg110 shows similar increase in SSA (+2.4 m^2/g from 4.4 m^2/g) in the inlet slice as the tests at lower temperature, which increase with values between +1.7 and +2.4 m^2/g, but display an even higher value in slice 3 (+3.5 m^2/g to 7.9 m^2/g). At the outlet (Fig. 1b) the value is the same as unflooded material for this core (4.8 m^2/g).

The SSA values for the two cores flooded at 130 °C behaves somewhat different from the other $MgCl_2$-flooded cores. In the core flooded the shortest time, 60 days, the SSA increased in all measured slices, with a peak in slice 7 (+4.6 m^2/g to 9.0 m^2/g), while the other two slices show increases of +2.9 m^2/g (slice 1) and +4.0 m^2/g (slice 3), compared to unflooded material from the same core (3.8 m^2/g). In the long-term test, L*Mg130*, the SSA peak appears in slice 3 (+2.8 m^2/g

Table 5
Core properties, saturated weight ($M_{sat,end}$), dry weight ($M_{dry,end}$), bulk volume ($V_{b,end}$), volumetric strain (ε_{vol}), and porosity estimation $\phi_{1,end}$, $\phi_{2,end}$ and $\phi_{3,end}$ after flooding, permeability at starting point (k_{ref}) and end state (k), mass loss ($\Delta m = M_{dry,end} - M_{dry,o}$).

Core	Fluid	T	$M_{dry,end}$	$M_{sat,end}$	$V_{b,end}$	ϕ_i	ε_{vol}	$\phi_{1,end}$	$\phi_{2,end}$	$\phi_{3,end}$	k_{ref}	k	Δm
		(°C)	(g)	(g)	(cm^3)	(%)	(%)	(%)	(%)	(%)	(mD)	(mD)	(g)
Mg25	$MgCl_2$	25	106.0	139.5	73.9	47.9	4.2	45.6	45.3	45.9	1.916	0.753	−0.59
Mg60		60	108.8	141.4	72.9	46.8	6.5	43.1	44.7	44.5	1.201	0.557	−1.48
Mg92		92	108.5	139.9	71.8	47.1	8.9	41.9	43.7	43.8	0.977	0.223	−2.24
Mg110		110	99.9	128.1	65.3	47.4	12.8	39.7	43.2	43.1	1.643	0.04	−3.03
Mg130		130	108.2	135.2	67.2	47.2	16.3	36.9	40.2	40.4	0.755	0.011	−4.13
L*Mg130*		130	114.7	142.7	70.6	47.5	17.5	36.4	39.7	39.8	0.77	0.009	−5.14
Na130	NaCl	130	111.5	144.6	76.3	46.9	5.1	44.0	43.4	45.5	1.118	0.568	−1.51
L*Na130*		130	104	135	70.6	47.5	6.9	43.6	43.9	45.0	1.173	0.13	−2.19

compared the initial value of 4.9 m^2/g). Slices 1 and 7 have increased values of +1.9 m^2/g and +0.8 m^2/g, respectively, compared to 4.9 m^2/g.

3.9. Permeability estimation

Fig. 7 shows the evolution of normalized permeability (k' = k/k_ref) through time during the creep phase. The starting points in the plots are based on the permeability measurements k_ref at the end of hydrostatic loading, i.e. start of creep. Table 5includes the permeability of each core at starting point (k_ref) and end state (*k*). The permeability of L***Na130*** (decreased by 88%) reduced more than that of ***Na130*** (decreased by 49%). At the end of the creep phases, ***Mg60*** and ***Na130*** showed similar permeability reduction (***Mg60***: 58%, ***Na130***: 49%) and ***Mg92*** and L***Na130*** had similar decrease (***Mg92***: 77%, L***Na130***: 88%), while ***Mg25*** decreased by 61%. L***Mg130*** and ***Mg130*** showed good repeatability, with closely overlapping graphs in Fig. 7 and also, the most significant permeability reductions. In L***Mg130*** and ***Mg130*** (130 °C) the permeability reduced from 0.77 to 0.76 mD to ~ 0.009 and ~0.0119 mD, respectively, after ~ 32 days of creep compaction. ***Mg110*** also displayed permeability reduction, but not as severe as ***Mg130*** and L***Mg130***. In ***Mg110*** it took ~42 days to observe a strong reduction (97.6%), from 1.6 to ~0.04 mD. The experimental set-ups were dismantled and cleaned after the tests and no restrictions in the form of precipitation or transported material were found in the tubing or other experimental equipment. Thus, the strong increase in differential pressure was induced by flow restrictions inside the cores from the compaction and flooding processes.

3.10. Porosity estimation

The porosities at the end of the tests were calculated (see 3.10. ***Porosity estimation*** in 2. ***Experimental procedure***) and summarized in Table 5. For the NaCl flooded cores (130 °C). They each show variations by ~1–2 porosity units: ***Na130***: $\phi_{end,1}$; 44.0%; $\phi_{end,2}$: 43.4%; $\phi_{end,3}$: 45.5% and L***Na130***: $\phi_{end,1}$; 43.6%; $\phi_{end,2}$: 43.9%; $\phi_{end,3}$: 45.0%). For the two NaCl-tests, ***Na130*** and L***Na130***, the estimate $\phi_{end,1}$ ignoring chemistry is within the range of the other two estimates and the uncertainties of the measurements.

For the $MgCl_2$ flooded cores the estimates taking both chemical reactions and volumetric strain into account ($\phi_{end,2}$ and $\phi_{end,3}$) are generally similar, varying only by 0.2 units except for ***Mg25*** (0.6 units difference). The porosity reduction (difference between end porosity (average of $\phi_{end,2}$ and $\phi_{end,3}$) and initial porosity) increases with temperature: ***Mg25***: −2.3%; ***Mg60***: −2.2%; ***Mg92***: −3.4%; ***Mg110***: −4.2% ***Mg130***: −6.9%; L***Mg130***: −7.8%. The porosity estimate $\phi_{end,1}$ (not accounting for chemistry) deviates gradually more from $\phi_{end,2}$ and $\phi_{end,3}$ with increasing temperature, underestimating the porosity by several units. This indicates that there has been a net solid volume reduction for these cores.

4. Discussion

4.1. Chemistry, mineralogy and temperatures

In Aalborg chalk samples flooded with NaCl at 130 °C, no newly precipitated minerals were observed using FEG-SEM (Fig. 3, sup. mat. Figs. 1 and 2) or XRD (sup. mat. Fig. 9b and c), in agreement with previous studies (Andersen et al., 2017; Madland et al., 2011; Megawati et al., 2015; Wang et al., 2016). This also shows that we can use the NaCl test series as comparison for those with $MgCl_2$. The limited changes in the samples are reflected by only small amounts of Ca^{2+} and Si^{4+} in the effluents (Fig. 6a, c) with more or less unchanged whole rock geochemistry measurements (Table 3a). The two mentioned NaCl flooded cores had slightly higher solid density (L***Na130***: 2.69 g/cm^3; ***Na130***: 2.68 g/cm^3) near the inlet and same density (L***Na130***: 2.68 g/cm^3; ***Na130***: 2.67 g/cm^3) near the outlet compared to the initial solid density (L***Na130-U***: 2.68 g/cm^3; ***Na130-U***: 2.67 g/cm^3). Furthermore, the SSA values (L***Na130***: 1.8 m^2/g, ***Na130***: 2.1 m^2/g) near the inlet are close to values reported from pure chalk (Stevns Klint: 1.7 m^2/g after Hjuler and Fabricius, 2009), while near the outlet they (L***Na130***: 3.8 m^2/g; ***Na130***: 4.6 m^2/g) are closer to unflooded Aalborg material (4.4 m^2/g, Table 1). These changes along the cores can be explained by dissolution of the lighter phase opal-CT, resulting in increased density and decreased SSA, which is supported by FEG-SEM, SiO_2 geochemical measurements (Table 3) and effluent analysis (Fig. 6c). This indicates that opal-CT is a component prone to changes and contributes to a significant impact on the mineralogical core properties as exposed to NaCl at elevated temperatures, a fluid earlier seen upon as being inert towards chalk.

Kinetic rates of geochemical reactions, such as mineral dissolution and precipitation, are temperature-dependent and typically increase with temperature. Previous studies have shown that chalk is more reactive towards $MgCl_2$ (Nermoen et al., 2016) and seawater (Korsnes et al., 2008; Zhang et al., 2007) when temperature is increased, by observations of more Ca^{2+} produced and more Mg^{2+} retained during flooding. The present study made the same observations from effluent measurements (Fig. 6) for Aalborg chalk that bears reactive opal-CT, and further consistently documented increased MgO content in the core with increasing temperature as a result of flooding with $MgCl_2$, revealed in whole-rock geochemical measurements (Table 3b).

FEG-SEM of L***Mg130*** and ***Mg130*** (Fig. 4c, d, e, sup. mat. Figs. 7 and 8) and XRD (sup. mat. Fig. 9h and i) clearly show precipitation of rhomboidal magnesite crystals, comparable to previous studies (Hiorth et al., 2013; Madland et al., 2011; Megawati et al., 2015; Wang et al., 2016; Zimmermann et al., 2015). Stable oxygen isotope values measured in L***Mg130*** are significantly altered towards more negative (Table 3b), particularly in slice 1, thus pointing to new growth of carbonate minerals. Magnesite formation is accelerated by increasing temperature (e.g., Möller, 1989). From 80 to 120 °C, magnesite can be readily precipitated by a spiral growth mechanism (Saldi et al., 2009), but rates of magnesite precipitation are severely limited at temperatures below 60 °C due to the strong hydration of Mg^{2+} ions in solution (Hänchen et al., 2008). Rhomboidal magnesite crystals were not observed with FEG-SEM in the cores flooded at 25, 60, 92 and 110 °C (sup. mat. Figs. 3–6), even though the samples showed MgO enrichment after flooding (Table 3b). Certainly, this might be related to the small grain size of newly formed crystals. Magnesite crystals or other carbonate phases, such as possible Mg-rich calcite, are in many cases too small (< 100 nm) to be imaged and analysed by FEG-SEM-EDS and the amount too low for the applied analytical techniques, such as XRD. TEM-EDS (transmission electron microscopy – EDS) and TERS (tip enhanced Raman spectroscopy) coupled with AFM (atomic force microscopy) studies show that the minerals are of that small size and can be imaged at the same time when they are determined (Borromeo et al., 2017; Egeland et al., 2017; Minde et al., 2017).

Fournier (1973) reported that the solubility of silica minerals such as amorphous silica, opal-CT, quartz and chalcedony increases with temperature in the range 25–250 °C in water. Dissolved silica can react with Mg^{2+} to form minerals of the form $(MgO)_x$ $(SiO_2)_x$•$(H_2O)_x$ (x = variable) and the precipitation mechanism occurs faster, producing larger amounts at high temperatures (Meyers, 1975). The principal solid alteration products include quartz, chrysotile, talc, kerolite, calcite, kaolinite, smectite, and amorphous silicate material with spongy, smectite-like morphology, identified by transmission electron microscopy (TEM), selected-area electron diffraction (SAED), and X-ray analytical electron microscopy (AEM) at ~ 45 and ~70 °C (Gíslason et al., 1993; Gunnarsson et al., 2005). This confirms our observation of Si-Mg-bearing minerals in FEG-SEM, produced by chemical interactions of Si^{4+}, dissolved from the host rock, with the reactive injected brine $MgCl_2$. At higher temperature, flaky minerals containing both Si and Mg are widespread throughout the cores, but the amount is low at the

inlet of the cores flooded at 25 and 60 °C. In general, the amounts of the new mineral phase(s) were too low to be identified using XRD. In the other four $MgCl_2$-flooded cores, the quantity of Si-Mg minerals increases with increasing flooding temperature. However, effluent analyses showed that Si^{4+} production during $MgCl_2$ injection was higher at 92 and 110 °C than at 130 °C (Fig. 6c). In addition, the effluent from L***Mg130*** was oversaturated with Si^{4+} as such that SiO_2 even precipitated from the effluent (Fig. 4i, l). This is also reflected in the average SiO_2 concentrations in the flooded slices, which was the lowest for ***Mg92*** and ***Mg110***, 3.70 and 3.42 wt% respectively, significantly lower than the two cores flooded with $MgCl_2$ at 130 °C with values of 4.66 (***Mg130***) and 4.58 (L***Mg130***). We interpret this observation, as a result of superimposed dissolution and precipitation processes: the chemical reaction rates are higher at higher temperature; therefore, more calcite and SiO_2 dissolves, while on the other hand more magnesite and Si-Mg-bearing minerals precipitate, as also observed by FEG-SEM. Hence, the cores flooded at 130 °C produced a lower net amount of Si^{4+} than at 92 and 110 °C.

Geochemical analyses and FEG-SEM-EDS measurements show the strongest enrichments in MgO in slice 2 in ***Mg130*** and L***Mg130***, while the other cores show the highest amount of MgO in slice 1. However, at 130 °C, there is also observed an increasing trend in SiO_2 and SSA accompanying MgO from slice 1 and further along the flooding axis of the core, both indications of precipitation of Si-Mg clay minerals. As more negative stable oxygen isotope values, in this study linked to newly precipitated carbonates, are observed in slice 1, it is likely to deduce that the magnesite precipitation peaks in slice 1. In both the high-temperature cores, an increase in flaky clay-minerals are observed, by FEG-SEM, increasing from the inlet towards the outlet of the cores, indicating that clay mineral precipitation has a peak further into the cores. As the clay minerals observed are Si-Mg minerals, the strong enrichment of MgO in slice 2 may originate from a combination of magnesite and clay-minerals. In previous studies and for the cores flooded at lower temperatures (where dissolution of opal-CT and precipitation of new Si-Mg clay minerals is less reactive) the peak in MgO is observed in slice 1. The enrichment of MgO in slice 2 is most visible in the longer of the two tests (Table 3b), and together with variations in SiO_2 profiles in the cores, may suggest that the interplay between the non-equilibrium brine, the rock and precipitated minerals together with the distribution of minerals are time-dependent processes (Minde et al., 2017).

Newly formed carbonate minerals, such as magnesite (3.0 g/cm^3) and Mg-rich calcite have higher density than calcite (2.71 g/cm^3). Precipitation of these minerals as well as of possible talc (2.76 g/cm^3) and dissolution of opal-CT (2.09 g/cm^3) are possibly the main processes leading to increased solid density at 60, 92, 110 and 130 °C. At 25 °C, limited dissolution of opal-CT and calcite results in only a small increase in solid density (Table 3b).

The changes in mineralogy with temperature are also reflected in the specific surface area (SSA) measurements. The precipitation of flaky Si-Mg-bearing phyllosilicates balances the reduction of the SSA by the dissolution of opal-CT lepispheres, both having significantly higher SSA than calcite. In the inlet slice, SSA increases more when going from 25 to 130 °C; correspondingly, ***Mg25***, which undergoes the least chemical reactions, gained the smallest increase in SSA. The SSA might also increase due to the formation of nano-sized magnesite and possible high-Mg calcite crystals. SSA slightly decreases near the outlet of the cores tested at 25, 60 and 92 °C. This may be explained by dissolution of opal-CT and calcite, accompanied by only limited precipitation as indicated by FEG-SEM (sup. mat. Figs. 3g, 4g and 5g). The data from this study shows that in increase in SSA, combined with an increase in SiO_2 and observed textural alterations by FEG-SEM, can be linked to higher abundances of newly formed clay-minerals, balancing dissolution of opal-CT. Additionally, presence of minute magnesite is believed to increase the SSA even more. L***Mg130*** has a smaller increase of SSA values, compared to unflooded material of the same core, than ***Mg130***. FEG-SEM micrographs comparing these cores show that in the core flooded for the longer time, larger magnesite crystals are formed, most likely due to the time aspect together with effects of Oswald ripening. This confirms that precipitation of magnesite also impacts SSA values. It should be noted that in Aalborg chalk, the original concentration of opal-CT and precipitation of euhedral magnesite crystals are influenced by the presence of larger pore-spaces, formed by foraminifera microfossils. These fossils are present throughout all tested cores, but vary strongly in abundance, and may therefore affect measurements of composition, SSA and density within each core.

4.2. Creep compaction and chemistry

During the primary creep compaction phase (~10 days, Fig. 5b), ***Mg25***, ***Mg60*** and ***Mg110*** showed higher creep rates than ***Mg92***, ***Mg130***, L***Mg130***, L***Na130*** due to the higher compaction rates towards the end of the hydrostatic loading (Fig. 5a). Loading phase effects were negligible in the following period (the remaining test time), and the $MgCl_2$-flooded cores then experienced higher compaction rates (Fig. 5b) with increasing temperatures. $MgCl_2$-flooded chalk cores compacted more than NaCl-flooded cores at 130 °C, in agreement with previous reports (Madland et al., 2011; Megawati et al., 2015; Wang et al., 2016). ***Mg25*** and ***Mg60*** obtained higher creep rates in the primary creep phase, and therefore show a high overall compaction.

NaCl-flooded cores at 130 °C behave similar to the ones, ***Mg25 and Mg60***, which have been injected by $MgCl_2$-brine at low temperature with low compaction rates (L***Na130***: 0.013%/day; ***Na130***: 0.013%/day; ***Mg25***: 0.015%/day; ***Mg60***: 0.015%/day). The chemical reactivity is low and dominated by weak dissolution. Mechanical deformation under effective stress is therefore the governing process during compaction.

The cores flooded with $MgCl_2$ at 92, 110 and 130 °C systematically showed higher compaction rates (***Mg92***: 0.029%/day; ***Mg110***: 0.039%/day; L***Mg130***: 0.045%/day; ***Mg130***: 0.052%/day). A similar trend was observed when flooding Obourg chalk (Mons, Belgium) with $MgCl_2$ at 92 and 130 °C (Nermoen et al., 2016). The rate of deformation with time is strongly linked to chemical alterations when injecting $MgCl_2$ at 130 °C (Megawati et al., 2015; Nermoen et al., 2015; Wang et al., 2016) since relatively inert brines such as NaCl result in much less compaction. Solid volume reduction induced by dissolution may affect the bulk volume directly. There are strong chalk-fluid interactions reducing the strength of particle bonds (Risnes, 2001). The dominating mechanism underlying the rate-type creep model is the off-sliding asperities under friction between granular contacts (Andersen et al., 1992; Anderson, 1995). Rounding of calcite grains by dissolution may decrease the intergranular friction and increase the probability for the grains to 'unlock' from their current organization and shift into nearby pores, thus effectively promoting the creep mechanisms.

Newly formed secondary minerals can trigger enhanced dissolution. On the other hand, the Mg-bearing minerals, particularly the flaky Si-Mg-bearing minerals, can act as contact cementation and strengthen the grain contacts, thus increasing the resistance against deformation (Olsen, 2007; Wetzel, 1989). However, this does not seem to be the case in our study, as increased strain is observed along with an increase in clay content after flooding.

4.3. Permeability evaluation

In brine-chalk systems, the permeability evolution is mainly affected by two coupled mechanisms: mechanical compaction and chemical alteration. This study shows that chemical reactions are weak at 25 and 60 °C when injecting $MgCl_2$ and at 130 °C when flooding with NaCl. Consequently, permeability reduction was lower in these cores than in cores tested at high temperature (Table 5). Permeability was reduced slightly more in the core flooded for a long time (L***Na130***) than in the core tested for a shorter period (***Na130***). Therefore, mechanical

compaction seems to be the dominant factor controlling permeability in ***Mg25*** and ***Mg60*** and the two NaCl flooded cores at higher temperatures (130 °C).

The cores tested at higher temperatures (110 and 130 °C) flooded with $MgCl_2$ showed significant permeability reductions (L***Mg130***: 98.8%; ***Mg130***: 98.5%; ***Mg110***: 97.6%) and the strong reduction in permeability is most likely related to the chemical reactions in the cores. FEG-SEM analyses show precipitation of Si-Mg-bearing minerals with thin flaky appearance. These minerals can cover significant portions of the pore surfaces and throats (Fig. 8), effectively reducing the permeability. Therefore, the dominating factor in the permeability development at higher temperature is chemical reactions, especially the formation of Si-Mg-bearing minerals. The formation of these minerals are dependent on a source of Si^{4+}, in this case, the abundant opal-CT.

Nermoen et al. (2015) observed that the permeability in a Liège chalk core (flooded with $MgCl_2$ at 130 °C) started to increase during a period between 140 and 160 days of flooding, after decreasing during the first ~112 days. This observation is different from ours, and most likely caused by the difference in flooding rates, primary mineralogy, with quartz representing the main non-carbonate phase in Liège chalk (Hjuler and Fabricius, 2009; Wang et al., 2016) instead of very fragile opal-CT, like in this study, besides the differences of absolute abundance of silica. Hence, the permeability development is strongly dependent on the presence of specific non-carbonate phases and their abundances as well as their stability and other mineralogical characteristics (e.g. form, surface charge, etc.).

4.4. Porosity evaluation

The three porosity estimates (see section 2.12. Porosity estimation) after flooding are calculated (Table 5) and plotted versus test temperature (Fig. 9). For the cores flooded with $MgCl_2$ at 25 °C and the two NaCl flooded cores (L***Na130*** and ***Na130***), there were no significant differences between the porosity estimates ignoring chemical reactions ($\phi_{end,1}$) and the porosity estimates taking the chemistry into account ($\phi_{end,2}$ and $\phi_{end,3}$) (Fig. 9; and according to Wang et al., 2016). Geochemical analyses, FEG-SEM and effluent measurements indicated limited chemical interaction and correspondingly minor changes in solid density and solid volume for these three cores, and the volumetric deformation was also low (Table 5). Therefore, mechanical compaction seems to be the main factor causing porosity reduction (Eq. (6)) in these cores.

From 60 to 130 °C, more volumetric compaction was observed in the $MgCl_2$ flooded cores (Fig. 5). Solid volume changes are related to calcite and opal-CT dissolution and precipitation of secondary minerals. As expected, the estimates $\phi_{end,2}$ and $\phi_{end,3}$ are generally similar, as they both are based on measuring porosity directly. With increasing temperatures, the porosity estimated by $\phi_{end,1}$ is increasingly imprecise, giving too low values, indicating that pore volume reduction alone does not explain the bulk volume changes, but rather that the solid volume also changes significantly. In particular, this estimate being systematically lower than the others, indicates a net reduction of the solid volume.

From 60 to 130 °C, the measured mass loss of the cores ($\Delta m = M_{dry,end} - M_{dry,o}$, ***Mg60***: −1.48 g; ***Mg92***: −2.24 g; ***Mg110***: −3.03 g; ***Mg130***: −4.13 g; L***Mg130***: −5.14 g, Table 5) becomes larger with increasing temperature due to stronger chemical reaction rates. Referring to Eqs. (6) and (10), a lower value of $\phi_{end,1}$ than $\phi_{end,2}$ and $\phi_{end,3}$ is indicative of $\Delta V_s < 0$. The loss of mass is consistent with an increasing deviation of $\phi_{end,1}$ from the two other estimates and a higher net dissolution of volume with higher temperature. It is known that Mg-Ca substitutions could cause a significant mass removal. However, we have observed a discrepancy between the measured mass loss ($M_{dry,end} - M_{dry,o}$) and the estimated core mass loss (from Mg^{2+} retention in the cores and Ca^{2+} production in the effluent, ***Mg60***: −0.25 g; ***Mg92***: −0.35 g; ***Mg110***: −0.64 g; ***Mg130***: −1.01 g; L***Mg130***: −1.50 g). The mismatch in mass loss may rather be strongly linked to calcium carbonate dissolution, as proposed by Nermoen et al. (2015) as well as, in this case, opal-CT ($SiO_2 \cdot H_2O$) dissolution. The exact explanation for the significant mass loss requires more detailed analysis of the newly formed minerals and pH changes in the effluent samples during the testing period and will not be part of this study, but rather a topic for future research.

We discussed earlier that at higher temperatures not only precipitation of higher density minerals, such as Mg-bearing minerals (magnesite: 3.0 g/cm^3), but also dissolution of low density minerals (opal-CT: 1.9–2.3 g/cm^3) may increase the solid density. The increased density, together with the decreased dry mass is the cause of the strong reduction in solid volume. These observations suggest that the dominating porosity reduction mechanisms at high temperature are chemical reactions; partly related to Mg-bearing minerals.

4.5. Application of the results

In the presented study, Aalborg cores were tested under specific North Sea reservoir temperatures (Valhall Field, 92 °C and Ekofisk Field, 130 °C), and compared with varying temperatures approaching surface conditions, e.g. injection well temperatures (25, 60, 110 °C) in a series of tests. The presence of opal-CT in chalk when flooding with non-equilibrium brines has a major effect on the permeability, as well as on the intensity of mineralogical changes. Even though the North Sea reservoir chalk does not commonly contain much opal-CT, it does contain abundant quartz, and it is believed that opal-CT is the source of this content created through diagenetic processes (Fabricius and Borre, 2007; Hjuler, 2007). Temperature dependent chemical reactions can induce changes in mineralogy, permeability and porosity in chalk. This is of relevance when using fluid injection for improved or enhanced oil recovery (EOR) in silica-rich reservoir chalk. Our serial laboratory experiments investigating chalk–brine interactions are paramount for prediction of effects related to non-carbonate phases, particularly opal-CT. Additionally, dissolution of other silicate phases, may produce similar Si^{4+} concentrations in pore-fluids and initiate similar precipitation-reactions as seen in this study. In field application, there will always be a temperature gradient between the injector and producer and it is thus important to characterize the chemo-mechanical interactions as function of temperature. The presented series of experiments may be helpful in predicting reservoir behaviour in terms of changes in mineralogy, permeability and porosity in chalk reservoirs, hence is important for all modelling exercises.

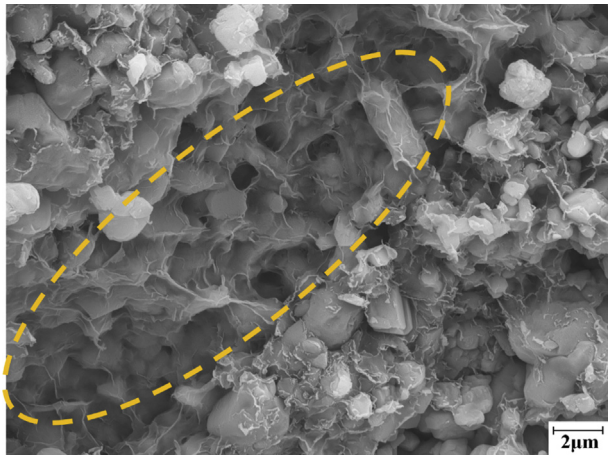

Fig. 8. FEG-SEM image of flooded L***Mg130*** (slice 6), showing pore surfaces and throats covered by newly formed Si-Mg-bearing minerals (orange dashed circle). (For interpretation of the references to colour in this figure legend, the reader is referred to the Web version of this article.)

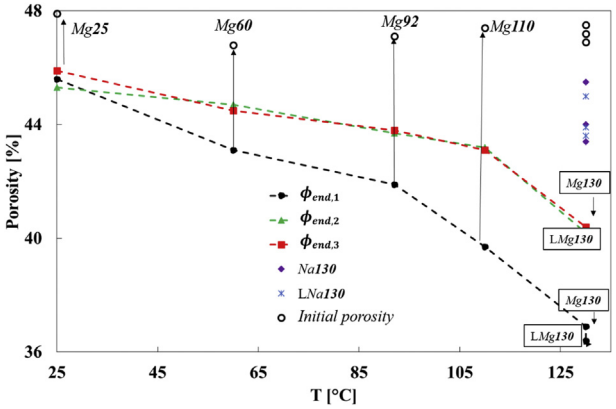

Fig. 9. Porosity values ($\phi_{end,1}$, $\phi_{end,2}$, $\phi_{end,3}$) of each flooded core (***Mg25***, ***Mg60***, ***Mg92***, ***Mg110***, ***Mg130***, L***Mg130***, L***Na130*** and ***Na130***) versus applied temperatures.

5. Conclusions

In previous works selected outcrop chalks have been studied in terms of rock mechanical behaviour and chemical interactions when flooding various brines or more general fluids to gain information related to enhanced oil recovery (EOR) in the North Sea. Reservoir chalks and some on-shore chalks contain high amounts of SiO_2, but the role of silicates in rock-fluid interactions has not yet been fully understood.

For the first time, a systematic study is presented on silica-rich (3.5 – 6 wt percent) reactive chalk from Aalborg (Denmark) flooded in experiments under a variety of different temperatures comparable to the reservoir and injection well conditions in the North Sea. The cores were flooded with 0.219 mol/L $MgCl_2$ or 0.657 mol/L NaCl brine at North Sea reservoir temperatures (Valhall field, 92 °C and Ekofisk field, 130 °C) and other temperatures (25, 60 and 110 °C) in a series of triaxial tests over 2 – 4 months. The NaCl flooded cores (flooded at 130 °C only) show comparable creep rates as $MgCl_2$ flooded cores tested at 25 and 60 °C. Cores flooded with $MgCl_2$-brine show systematically higher creep rates at increasing temperatures.

Effluent profiles show that calcite and opal-CT dissolution and magnesium retention increase with increasing temperatures, supported by whole-rock geochemical analyses, FEG-SEM-EDS, XRD and solid density measurements. After flooding with $MgCl_2$ at 110 and 130 °C newly formed magnesite is observed, size and abundance increasing with temperature and time. In the cores tested at temperatures 25, 60 and 92 °C, magnesite crystals have not been positively identified but an increase in MgO in whole-rock analyses is detected. Simultaneously, silica-distribution is altered by flooding, both through dissolution of silica-bearing phases, primary opal-CT, and precipitation of Mg-Si-bearing minerals, identified by whole-rock geochemistry, effluent measurements and FEG-SEM-EDS.

Our findings suggest that the presence of reactive opal-CT in Aalborg chalk plays a crucial role in the temperature range from 25 to 130 °C. The Si^{4+} ions obtained by dissolution of silicate-bearing phases allow for interaction with Mg^{2+} in the brine, resulting in precipitation of Si-Mg-bearing minerals, which in turn affected the SSA, precipitation of other minerals and changes in geo-mechanical parameters.

A novel observation for opal-CT bearing chalk was the identification, by FEG-SEM-EDS, of significant re-precipitation of Si-Mg-bearing minerals during $MgCl_2$ injection at all temperatures; distributed throughout the cores tested at 92, 110 and 130 °C, but only near the inlet of the cores tested at 25 and 60 °C. Specific surface area (SSA) increases accordingly in the $MgCl_2$ flooded cores, as expected, caused by the formation of flaky Si-Mg-bearing minerals and minute magnesium bearing carbonate crystals during the tests at mentioned temperatures; however, in NaCl flooded cores dissolution of silica-bearing phases, mainly opal-CT, can alter the distribution of silica and reduce the SSA. Consequently, the processes of dissolution of silicate and calcite and re-precipitation as magnesite, Mg-Si-bearing minerals and possibly other Mg-rich minerals are the dominant control for the strong reduction (> 90%) in permeability for the $MgCl_2$ flooded cores at higher temperatures (92, 110 and 130 °C). The temperature effects on chemical alterations are also reflected in the porosity evolution. With increasing temperature, chemical alterations play an increasingly significant role, based on deviations in porosity estimates solely based on pore volume reduction, compared to direct calculations of porosity after flooding. The presence of opal-CT affects the distribution of MgO in the flooded cores, especially at high temperature. This shows the increased complexity of chemical reactions and in equilibrium states when adding relatively small amounts (3.5–6.0 wt%) of reactive silica-phases.

This study confirms that in brine-rock systems, temperature, together with the original composition (mineralogy), are active factors in controlling chemo–mechanical interactions. Specifically, siliceous phases in the form of opal-CT reacts actively towards $MgCl_2$ and significantly influence permeability. The results from this study should be taken into consideration when predicting the mechanical behaviour and mineralogical changes during brine injection in reservoir under various temperatures.

Acknowledgements

The authors thank the Faculty of Science and Technology at UiS for the PhD grant for Wenxia Wang and the National IOR Centre of Norway for the PhD grant for Mona Wetrhus Minde. We are grateful to Tania Hildebrand-Habel for the FEG-SEM work on two of the cores (Mg130, LMg130). The authors thank COREC and also acknowledge the Research Council of Norway (230303) and the industry partners; ConocoPhillips Skandinavia AS, Aker BP ASA, Eni Norge AS, Maersk Oil Norway AS, DONG Energy A/S, Denmark, Statoil Petroleum AS, ENGIE E&P NORGE AS, Lundin Norway AS, Halliburton AS, Schlumberger Norge AS, Wintershall Norge AS, DEA Norge AS of The National IOR Centre of Norway for support.

The research presented is integral part of the PhD theses of Mona Wetrhus Minde and Wenxia Wang at UiS.

Appendix A. Supplementary data

Supplementary data related to this article can be found at http://dx.doi.org/10.1016/j.petrol.2018.05.072.

References

Andersen, M.A., Foged, N., Pedersen, H.F., 1992. The rate- type compaction of a weak North Sea chalk. In: Wawersik, T. (Ed.), Rock Mechanics. Balkema, Rotterdam.

Andersen, P.Ø., Evje, S., Madland, M.V., Hiorth, A., 2012. A geochemical model for interpretation of chalk core flooding experiments. Chem. Eng. Sci. 84, 218–241. http://dx.doi.org/10.1016/j.ces.2012.08.038.

Andersen, P.Ø., Evje, S., 2016. A model for reactive flow in fractured porous media. Chem. Eng. Sci. 145, 196–213. http://dx.doi.org/10.1016/j.ces.2016.02.008.

Andersen, P.Ø., Wang, W., Madland, M.V., Zimmermann, U., Korsnes, R.I., Bertolino, S.R.A., Minde, M.W., Schulz, B., Gilbricht, S., 2017. Comparative study of five outcrop chalks flooded at reservoir conditions: chemo-mechanical behaviour and profiles of compositional alteration. Transport Porous Media 1–47. http://dx.doi.org/10.1007/s11242-017-0953-6.

Anderson, T.F., Arthur, M.A., 1983. Stable isotopes of oxygen and carbon and their application to sedimentologic and environmental problems. In: Arthur, M.A., Anderson, T.F., Kaplan, I.R., Veizer, J., Land, L.S. (Eds.), Stable Isotopes in Sedimentary Geology. Society of Economic Paleontologists and Mineralogists, Short Course Notes. vol. 10 1−151.

Anderson, T.L., 1995. Fracture Mechanics: Fundamentals and Applications, second ed. CRC Press, Boca Raton.

André, L., Audigane, P., Azaroual, M., Menjoz, A., 2007. Numerical modeling of fluid–rock chemical interactions at the supercritical CO_2–liquid interface during CO_2 injection into a carbonate reservoir, the Dogger aquifer (Paris Basin, France). Energy Conversion and Mangement 48, 1782–1797. http://dx.doi.org/10.1016/j.enconman.2007.01.006.

Bertolino, S.R., Zimmermann, U., Madland, M.V., Hildebrand-Habel, T., Hiorth, A., Korsnes, R.I., 2013. Mineralogy, geochemistry and isotope geochemistry to reveal fluid flow processes in flooded chalk under long term test conditions for EOR purposes. In: XV International Clay Conference, Brasil, pp. 676.

Borromeo, L., Minde, M.W., Zimmermann, U., Andò, S., toccafondi, c, Ossikovski, R., 2017. A new frontier technique for nano-analysis on flooded chalk: TERS (Tip Enhanced Raman Spectroscopy). In: EAGE - 19th European Symposium on Improved Oil Recovery. University of Stavanger.
Bromley, R.G., 1968. Burrows and borings in hardgrounds. Medd. Dansk Geol.Foren. 18, 247–250.
Brunauer, S., Emmett, P.H., Teller, E., 1938. Adsorption of gases in multimolecular layers. J. Am. Chem. Soc. 60, 309–319. http://dx.doi.org/10.1021/ja01269a023.
Crittenden, J.C., Trussell, D.W., Hand, K.J., Howe, G., Tchobanoglous, G., 2012. MWH's Water Treatment: Principles and Design, third ed. .
Egeland, N., Minde, M.W., Kobayashi, K., Ota, T., Nakamura, E., Zimmermann, U., Madland, M.V., Korsnes, R.I., 2017. Quantification of mineralogical changes in flooded carbonate under reservoir conditions. In: 19th European Symposium on Improved Oil Recovery/IOR Norway 2017, Stavanger.
Elraies, K.A., Basbar, A.E.A., 2015. The effect of water salinity on silica dissolution rate and subsequent formation damage during chemical EOR process. Petroleum & environmental biotechnology 6, 1–6. http://dx.doi.org/10.4172/2157-7463.100020906.
Evje, S., Hiorth, A., Madland, M.V., Korsnes, R.I., 2009. A mathematical model relevant for weakening of chalk reservoirs due to chemical reactions. Netw. Heterogeneous Media 4 (4), 755–788.
Fabricius, I.L., 2001. Compaction of microfossil and clay-rich chalk sediments. Phys. Chem. Earth Part a Solid Earth and Geodesy 26, 59–62.
Fabricius, I.L., Hoier, C., Japsen, P., Korsbech, U., 2007. Modelling elastic properties of impure chalk from South Arne field. North Sea. Geophys. Prospect 55, 487–506.
Fabricius, I.L., Borre, M.K., 2007. Stylolites, porosity, depositional texture, and silicates in chalk facies sediments. Ontong Java Plateau–Gorm and Tyra fields, North Sea. Sedimentology 54, 183–205.
Fjær, E., Holt, R.M., Horsrud, P., Raaen, A.M., Risnes, R., 2008. Petroleum Related Rock Mechanics, second ed. Elsevier, Amsterdam, Netherlands, pp. 491–492.
Fournier, R.O., 1973. Silica in thermal water: laboratory and field investigations. In: Proceedings of the International Symposium on Hydrogeochemistry and Biochemistry. vol. 1. pp. 122–139.
Gíslason, S.R., Veblen, D.R., Livi, K.J.T., 1993. Experimental meteoric water-basalt interaction-Characterization and interpretation of alteration products. Geochem. Cosmochim. Acta 57, 1459–1471. http://dx.doi.org/10.1016/0016-7037(93)90006-I.
Green, D.W., Willhite, G.P., 1998. Enhanced oil recovery. In: Henry, L. (Ed.), Doherty Memorial Fund of AIME. Society of Petroleum Engineers, Richardson, TX.
Gunnarsson, I., Arnórsson, S., Jakobbsson, S., 2005. Precipitation of poorly crystalline antigorite under hydrothermal conditions. Geochem. Cosmochim. Acta 69, 2813–2828. http://dx.doi.org/10.1016/j.gca.2005.02.001.
Hellmann, R., Renders, P., Gratier, J., Guiguet, R., 2002. Experimental pressure solution compaction of chalk in aqueous solutions Part 1. Deformation behavior and chemistry. In: Hellmann, R., Wood, S.A. (Eds.), Water-rock Interactions, Ore Deposits, and Environmental Geochemistry: a Tribute to Davod a. Crerar. vol. 7. pp. 129–152.
Hermansen, H., Thomas, L.K., Sylte, J.E., Aasboe, B.T., 1997. Twenty Five Years of Ekofisk Reservoir Management. pp. 873–885. http://dx.doi.org/10.2118/38927-ms.
Hermansen, H., Landa, G.H., Sylte, J.E., Thomas, L.K., 2000. Experiences after 10 years of waterflooding the Ekofisk field, Norway. J. Petrol. Sci. Eng. 26, 11–18.
Hiorth, A., Jettestuen, E., Cathles, L.M., Madland, M.V., 2013. Precipitation, dissolution, and ion exchange processes coupled with a lattice Boltzmann advection diffusion solver. Geochem. Cosmochim. Acta 104, 99–110. http://dx.doi.org/10.1016/j.gca.2012.11.019.
Hjuler, M.L., 2007. Diagenesis of Upper Cretaceous Onshore and Offshore Chalk from the North Sea Area. PhD thesis. Technical University of Denmark.
Hjuler, M.L., Fabricius, I.L., 2009. Engineering properties of chalk related to diagenetic variations of Upper Cretaceous onshore and offshore chalk in the North Sea area. J. Petrol. Sci. Eng. 68, 151–170. http://dx.doi.org/10.1016/j.petrol.2009.06.005.
Hänchen, M., Prigiobbe, V., Baciocchi, R., Mazzotti, M., 2008. Precipitation in the Mg-carbonate system-effects of temperature and CO_2 pressure. Chem. Eng. Sci. 63 (4), 1012–1028.
Korsnes, R.I., Strand, S., Hoff, Ø., Pedersen, T., Madland, M.V., Austad, T., 2006a. Does the chemical interaction between seawater and chalk affect the mechanical properties of chalk. In: The International Symposium of the International Society for Rock Mechanics, http://dx.doi.org/10.1201/9781439833469.ch61.
Korsnes, R.I., Madland, M.V., Austad, T., 2006b. Impact of brine composition on the mechanical strength of chalk at high temperature. In: The International Symposium of the International Society for Rock Mechanics. Liége, Belgium, http://dx.doi.org/10.1201/9781439833469.ch18.
Korsnes, R.I., Madland, M.V., Austad, T., Haver, S., Røsland, G., 2008. The effects of temperature on the water weakening of chalk by seawater. J. Petrol. Sci. Eng. 60, 183–193. http://dx.doi.org/10.1016/j.petrol.2007.06.001.
Kristiansen, T.G., Barkved, O.I., Buer, K., Bakke, R., 2005. Production-induced deformations outside the reservoir and their impact on 4D seisimic. International Petroleum Technology Conference 1–12. http://dx.doi.org/10.2523/IPTC-10818-MS.
Lauridsen, B.W., Surlyk, F., Bromley, R.G., 2011. Trace fossils of a cyclic chalk–marl succession; the upper Maastrichtian Rørdal Member, Denmark. Cretac. Res. 32, 194–202. http://dx.doi.org/10.1016/j.cretres.2010.12.002.
MacDonald, Gordon J.F., 1956. Experimental determination of calcite-aragonite equilibrium relations at elevated temperatures and pressures. Am. Mineral. 41, 744–756.
Madland, M.V., Midtgarden, K., Manafov, R., Korsnes, R.I., Kristiansen, T.G., Hiorth, A., 2008. The effect of temperature and brine composition on the mechanical strength of Kansas chalk. In: International Symposium of the Society of Core Analysts. Abu Dhabi.
Madland, M.V., Hiorth, A., Omdal, E., Megawati, M., Hildebrand-Habel, T., Korsnes, R.I., Evje, S., Cathles, L.M., 2011. Chemical alterations induced by rock–fluid interactions when injecting brines in high porosity chalks. Transport Porous Media 87, 679–702. http://dx.doi.org/10.1007/s11242-010-9708-3.
McLennan, S.M., Taylor, S.R., Hemming, S.R., 2006. Composition, differentiation, and evolution of continental crust: constraints from sedimentary rocks and heat flow. In: Brown, M., Rushmer, T. (Eds.), Evolution and Differentiation of the Continental Crust. Cambridge Univ Press, Cambridge, pp. 92–134.
Megawati, M., Andersen, P.Ø., Korsnes, R.I., Evje, S., Hiorth, A., Madland, M.V., 2011. The effect of aqueous chemistry pH on the time-dependent deformation behavior of chalk experimental and modelling study. In: Pore2Fluid International Conference. 16–18 Nov, Paris, France.
Megawati, M., Hiorth, A., Madland, M.V., 2013. The Impact of surface charge on the mechanical behaviour of high-porosity chalk. Rock Mech. Rock Eng. 46, 1073–1090. http://dx.doi.org/10.1007/s00603-012-0317-z.
Megawati, M., Madland, M.V., Hiorth, A., 2015. Mechanical and physical behavior of high-porosity chalks exposed to chemical perturbation. J. Petrol. Sci. Eng. 133, 313–327. http://dx.doi.org/10.1016/j.petrol.2015.06.026.
Meyers, P., 1975. Behaviour of silica in ion exchange and other systems. In: The International Water Conference, Pittsburgh, March. 1–10.
Minde, M.W., Haser, S., Korsnes, R.I., Zimmermann, U., Madland, M.V., 2017. Comparative studies of mineralogical alterations of three ultra-long-term tests of onshore chalk at reservoir conditions. In: 19th European Symposium on Improved Oil Recovery/IOR NORWAY 2017, Stavanger.
Möller, P., 1989. Magnesite : geology, mineralogy, geochemistry, formation of Mg-carbonates. In: Möller, P. (Ed.), Monograph Series on mineral Deposits. 28 1–300.
Nagel, N.B., 2001. Compaction and subsidence issues within the petroleum industry: from Wilmington to Ekofisk and beyond. Phys. Chem. Earth Solid Earth Geodes. 26, 3–14. http://dx.doi.org/10.1016/S1464-1895(01)00015-1.
Nermoen, A., Korsnes, R.I., Hiorth, A., Madland, M.V., 2015. Porosity and permeability development in compacting chalks during flooding of nonequilibrium brines: insights from long-term experiment. Journal of Geophysical Research-Solid Earth 120, 2935–2960. http://dx.doi.org/10.1002/2014JB011631.
Nermoen, A., Korsnes, R.I., Aursjø, O., Madland, M.V., Kjørslevik, T.A.C., Østensen, G., 2016. How stress and temperature conditions affect rock-fluid chemistry and mechanical deformation. Frontiers in Physics 4, 1–19. http://dx.doi.org/10.3389/fphy.2016.00002.
Newman, G.H., 1983. The effect of water chemistry on the laboratory compression and permeability characteristics of some North Sea chalks. J. Petrol. Technol. 35, 976–980. http://dx.doi.org/10.2118/10203-pa.
Olsen, C., 2007. Elastic and Electric Properties of North Sea Chalk. PhD thesis). .
Risnes, R., Flaageng, O., 1999. Mechanical properties of chalk with emphasis on chalk-fluid interactions and micromechanical aspects. Oil & Gas Science and Technology-Revue D Ifp Energies Nouvelles 54, 751–758. http://dx.doi.org/10.2516/Ogst:1999063.
Risnes, R., 2001. Deformation and yield in high porosity outcrop chalk. Phys. Chem. Earth Solid Earth Geodes. 26, 53–57. http://dx.doi.org/10.1016/S1464-1895(01)00022-9.
Risnes, R., Madland, M.V., Hole, M., Kwabiah, N.K., 2005. Water weakening of chalk-mechanical effects of water-glycol mixtures. J. Petrol. Sci. Eng. 48, 21–36. http://dx.doi.org/10.1016/j.petrol.2005.04.004.
Saldi, G.D., Jordan, G., Schott, J., Oelkers, Eric, H., 2009. Magnesite growth rates as a function of temperature and saturation state. Geochem. Cosmochim. Acta 73, 5646–5657.
Stenestad, E., 2006. Fluviokarst in the top of the Maastrichtian chalk at Rørdal, Northern Jutland. Denmark. Bull.. geo. Soc. Denmark 53, 93–110.
Surlyk, F., Stemmerik, L., Ahlborn, M., Harlou, R., Lauridsen, B.W., Rasmussen, S.L., Schovsbo, N., Sheldon, E., Thibault, N., 2010. The cyclic Rørdal Member-a new lithostratigraphic unit of chronostratigraphic and palaeoclimatic importance in the upper Maastrichtian of Denmark. Bull. Geol. Soc. Den. 58, 89–98.
Wang, W., Madland, M.V., Zimmermann, U., Nermoen, A., Korsnes, R.I., Bertolino, S.R.A., Hildebrand-Habel, T., 2016. Evaluation of Porosity Change during Chemo-mechanical Compaction in Flooding Experiments on Liège Outcrop Chalk. The Geological Society of Londonhttp://dx.doi.org/10.1144/SP435.10. Special publication.
Wetzel, A., 1989. Influence of heat flow on ooze/chalk cementation: quantification from consolidation parameters in DSDP Sites 504 and 505 sediments. J. Sediment. Petrol. 59, 539–547.
Wilson, M.J., 2014. The structure of opal-CT revisited. Journal of Non-Crustalline solids 405, 68–75. http://dx.doi.org/10.1016/j.jnoncrysol.2014.08.052.
Wright, E.K., 1987. Stratification and paleocirculation of the late cretaceous Western interior seaway of North America. Geol. Soc. Am. Bull. 99, 480–490. http://dx.doi.org/10.1130/0016-7606(1987)99<480:SAPOTL>2.0.CO;2.
Zhang, P., Tweheyo, M.T., Austad, T., 2007. Wettability alteration and improved oil recovery by spontaneous imbibition of seawater into chalk: impact of the potential determining ions Ca^{2+}, Mg^{2+}, and SO_4^{2-}. Colloid. Surface. Physicochem. Eng. Aspect. 301, 199–208. http://dx.doi.org/10.1016/j.colsurfa.2006.12.058.
Zimmermann, U., Madland, M.V., Bertolino, S.A.R., Hildebrand-Habel, T., 2013. Tracing fluid flow in flooded chalk under long term test conditions. In: 75th EAGE Conference & Exhibition Incorporating SPE. London.
Zimmermann, U., Madland, M.V., Nermoen, A., Hildebrand-Habel, T., Bertolino, S.A.R., Hiorth, A., Korsnes, R.I., Audinot, J.N., Grysan, P., 2015. Evaluation of the compositional changes during flooding of reactive fluids using scanning electron microscopy, nano-secondary ion mass spectrometry, x-ray diffraction and whole rock geochemistry. AAPG (Am. Assoc. Pet. Geol.) Bull. 99, 791–805. http://dx.doi.org/10.1306/12221412196.